AGU PUBLICATIONS

JGR

Journal of Geophysical Research: Atmospheres

RESEARCH ARTICLE
10.1002/2017JD027003

Key Points:
- The 3-D modeling of polar stratospheric clouds simulates two size modes of NAT that are inferred over Antarctica
- NAT nucleated from STS produces NAT particles with sizes near 8 μm, but NAT released from ice produces small NAT particles
- Adding temperature fluctuations is important to produce larger number densities and higher backscattering ratios from ice and NAT particles

Correspondence to:
Y. Zhu,
yunqian.zhu@colorado.edu

Citation:
Zhu, Y., Toon, O. B., Lambert, A., Kinnison, D. E., Bardeen, C., & Pitts, M. C. (2017). Development of a polar stratospheric cloud model within the Community Earth System Model: Assessment of 2010 Antarctic winter. *Journal of Geophysical Research: Atmospheres*, *122*. https://doi.org/10.1002/2017JD027003

Received 20 APR 2017
Accepted 18 SEP 2017
Accepted article online 25 SEP 2017

Development of a Polar Stratospheric Cloud Model Within the Community Earth System Model: Assessment of 2010 Antarctic Winter

Yunqian Zhu[1], Owen B. Toon[1], Alyn Lambert[2], Douglas E. Kinnison[3], Charles Bardeen[3], and Michael C. Pitts[4]

[1]Laboratory for Atmospheric and Space Physics, University of Colorado Boulder, Boulder, CO, USA, [2]Jet Propulsion Laboratory, California Institute of Technology, Pasadena, CA, USA, [3]National Center for Atmospheric Research, Boulder, CO, USA, [4]Langley Research Center, Hampton, VA, USA

Abstract To simulate polar stratospheric clouds (PSCs) during the Antarctic winter of 2010, we have developed a PSC model within the Community Earth System Model framework that includes detailed microphysics of sulfuric aerosols and three types of PSCs: supercooled ternary solution (STS), nitric acid trihydrate (NAT), and ice. Our model includes two major NAT formation mechanisms, both of which are essential to reproduce the PSC and gas phase chemical features in the 2010 Antarctic winter. Homogeneous nucleation of NAT from STS produces NAT particles with sizes near 8 μm, which are important to properly simulate denitrification and the gas phase HNO_3 observed by the Microwave Limb Sounder (MLS). Heterogeneous nucleation of NAT on ice particles or ice particles on NAT and subsequent evaporation of the ice produces NAT particles with sizes from submicrometers to a few micrometers. These particles account for the large backscattering ratio from NAT observed by the Cloud-Aerosol Lidar and Infrared Pathfinder Satellite Observations satellite, especially in the midwinter season. Adding temperature fluctuations from gravity waves is important to produce larger number density and higher backscattering ratio from ice and NAT particles. However, our model needs a better representation of waves to improve the backscattering ratio and gas phase HNO_3 compared with observations. Our model also includes homogeneous nucleation of ice from STS and heterogeneous nucleation of ice on NAT. The model reproduces the gas phase H_2O during the winter within the uncertainty of the MLS observations.

1. Introduction

Polar stratospheric clouds (PSCs) play critical roles in polar ozone depletion. Heterogeneous chemistry occurring on/in PSCs transfers chlorine and bromine from reservoir species into active species (Solomon et al., 1986). The active chlorine species are photolyzed by sunlight and participate in ozone destruction cycles. Falling PSC particles redistribute the HNO_3 and H_2O in the lower stratosphere, known as denitrification and dehydration, which also affects ozone depletion.

Temperature is one of the main factors that drive the formation of PSCs and determine their compositions. PSCs are usually classified in three categories: the solid phase nitric acid trihydrate (NAT) exists about 6–7 K above the ice frost point (Hanson & Mauersberger, 1988); the liquid phase supercooled ternary solution (STS) forms on the background sulfate aerosols as the temperature decreases, and significant mass is added approximately 3.5 K below the NAT equilibrium temperature (2.5–3.5 K above the ice frost point) (Carslaw et al., 1994); and the solid phase ice PSCs are crystalline particles containing a great amount of water ice (Turco, Toon, & Hamill, 1989), forming below the ice frost point (Poole & McCormick, 1988).

Previous studies suggest two major mechanisms for NAT formation in the Antarctic winter depending on the temperature (Zhu et al., 2017). In early winter before the temperature drops below the ice frost point (usually before the end of May), satellite observations (Lambert et al., 2012) suggest that denitrification is caused by NAT with low number densities ($<10^{-3}$ cm^{-3}) and large effective radius (>5–7 μm). This early winter denitrification as well as the NAT particle sizes and numbers are simulated within the uncertainty of the observations when NAT particles are assumed to be formed from STS through homogenous nucleation (Zhu et al., 2017). After the end of May, satellite observations and simulations demonstrate that NAT particles with sizes near 1 μm or smaller are released from ice clouds forming near the Antarctic Peninsula in mountain waves. These NAT particles spread downwind, creating a belt of NAT

around the periphery of the continent (Eckermann et al., 2009; Höpfner et al., 2006; Lambert et al., 2012) during June, July, and August. These small NAT particles may grow larger and denitrify the stratosphere if the temperature remains below the NAT equilibrium temperature for several days (Fueglistaler et al., 2002). Similar formation of NAT from ice in mountain waves has been observed in the Arctic from aircraft observations (Carslaw et al., 1998b).

Temperature fluctuations caused by gravity waves are observed and demonstrated to be associated with PSC formation (Höpfner et al., 2001) and ozone depletion (Carslaw et al., 1998a), especially in the Arctic winter. In the Antarctic, the cold interior of the vortex allows copious PSCs to form, but gravity waves still contribute a significant amount to PSC formation. Noel and Pitts (2012) analyze years from 2006 to 2010 and find that on average 36% of Antarctic days are orographic gravity wave active. Alexander et al. (2013) draw a similar conclusion with an analysis from 2007 to 2010. In the mountainous areas near the coast, over 75% of H_2O ice PSCs and around 50% of high number density STS/NAT mixtures, as defined by the Cloud-Aerosol Lidar and Infrared Pathfinder Satellite Observations (CALIPSO) PSC classification algorithm (Pitts, Poole, & Thomason, 2009), are attributed to orographic gravity wave activity (Alexander et al., 2013). Considering the entire Antarctic vortex a much smaller fraction (~5%) of PSCs was due to mountain waves (Alexander et al., 2013). Höpfner et al. (2006) show that small NAT particles may nucleate on ice particles in large-amplitude gravity waves.

In this paper, we evaluate simulations of PSCs using the Community Earth System Model, version 1 (CESM1), a global climate model maintained at the National Center for Atmospheric Research (NCAR) and sponsored by the U.S. Department of Energy and the National Science Foundation (NSF). These simulations include STS and NAT microphysics as described in Zhu et al. (2015, 2017). In addition, a new ice microphysical model replaces the prognostic treatment for ice PSCs in Zhu et al. (2015, 2017). We compare the simulated PSCs with and without gravity waves over the Antarctic mountains with observations for the 2010 Antarctic winter which was previously investigated by Zhu et al. (2017) with a simpler ice physics model.

The questions we investigate are the following:

1. Does the new model simulate PSCs with the sizes that are inferred over Antarctica?
2. Does the new model reproduce optical properties during different time periods (early winter and midwinter) as observed from CALIPSO?
3. How does the simulated denitrification and dehydration during the 2010 Antarctic winter compare with Microwave Limb Sounder (MLS) data?
4. When we add gravity waves, how do the size and optical properties of the particles, denitrification, and dehydration change?
5. Does adding gravity waves to the model change the ozone loss over Antarctica?

Below we first review the observational data we use for the analysis of the 2010 Antarctic winter, and then we present the details of the PSC model we have developed. Finally, we compare our simulations with data and address the five questions listed above.

2. Observations

Many satellite remote sensing measurements of PSCs and of Antarctic chemistry have been conducted since the end of the twentieth century. We use Cloud-Aerosol Lidar and Infrared Pathfinder Satellite Observations (CALIPSO) and Aura Microwave Limb Sounder (MLS) data to investigate the coverage, denitrification, and dehydration of PSCs throughout the Antarctic winter of 2010. MLS measures the nitric acid and water, rather than denitrification and dehydration. Denitrification and dehydration can be either irreversible or temporary. Irreversible indicates that the HNO_3 or H_2O permanently are removed from the air mass by sedimentation. Temporary occurs when the HNO_3 or H_2O are removed from the vapor phase and transferred to the condensed phase. "Temporary" means that the HNO_3 or H_2O in the particles can be released back to the gas phase once the particles evaporate.

2.1. CALIPSO

The Cloud-Aerosol Lidar with Orthogonal Polarization (CALIOP) instrument aboard the CALIPSO spacecraft is a two-wavelength, polarization-sensitive lidar that provides high-resolution profiles both of backscatter and

of polarization (Winker, Hunt, & McGill, 2007). For the lower stratosphere where PSCs often occur, the vertical resolution is as high as 60–180 m. CALIOP measures the backscatter coefficients at 532 and 1064 nm and two orthogonal (parallel and perpendicular) polarization components at 532 nm (Winker et al., 2007).

The CALIPSO PSC detection and classification algorithm was developed to provide detailed vertical and spatial distributions of PSCs and PSC composition classes (Pitts et al., 2007, 2009, 2013). The algorithm uses perpendicular backscatter coefficient, total backscattering ratio, and particulate depolarization ratio as the criteria to define the existence of PSCs and their composition classes (Pitts et al., 2009). The total backscattering ratio (R_{532}) is the ratio of total volume backscatter at 532 nm to the molecular backscatter coefficient at 532 nm. The particulate depolarization ratio (δ_{aerosol}) is the ratio of the perpendicular to parallel component of the particulate backscatter coefficient. The CALIPSO algorithm classifies PSCs into four main categories (STS, Mix1, Mix2, and ice) and two subcategories (Mix2-enhanced and wave ice). The STS category includes particles whose backscattering ratio exceeds a certain threshold and which have no detectable enhancement in perpendicular backscatter coefficient (Pitts et al., 2013). The Mix1, Mix2, and Mix2-enhanced categories are assumed to be NAT/STS mixtures with successively increasing backscatter. The backscattering ratio boundary between STS/NAT mixtures and STS/ice mixtures (the ice category) is assumed to be 5. The wave ice category includes particles with backscattering ratio larger than 50. The data are based on version 1 CALIOP level 2 PSC data products from the NASA Langley Atmospheric Science Data Center (http://eosweb.larc.nasa.gov/).

2.2. MLS

The Microwave Limb Sounder (MLS) on board NASA's Earth Observing System Aura satellite has been measuring the atmospheric composition, temperature, humidity, and cloud ice since 2004 (Schoeberl, 2007). We are interested in the temperature and gas phase abundances of HNO_3, H_2O, N_2O, and O_3 from 1 May to 31 October 2010. Livesey et al. (2011) provide the resolution, accuracy, and precision information for each constituent measured. For the lower stratosphere, the typical vertical resolution is 2–3.7 km for H_2O, 3–5 km for HNO_3, 4–6 km for N_2O, and 2.5 km for O_3. The MLS HNO_3 systematic error (accuracy) is ±0.25–0.5 ppbv for 100–32 hPa and ±0.5–1 ppbv for 22 hPa, and the random error (precision) is ±0.7 ppbv. For the vertical level 20–68 hPa, the MLS H_2O accuracy is 4–7% and the precision is 6–8%. For N_2O, the accuracy is 19–70 ppbv and the precision is 13–24 ppbv. For O_3, the accuracy is 0.05–0.2 ppmv and the precision is 0.04–0.1 ppmv (http://mls.jpl.nasa.gov/).

As A-Train satellites, MLS and CALIPSO share the same orbit, but the MLS measurements are several minutes behind CALIPSO's.

3. Model Description

Zhu et al. (2015, 2017) developed a PSC model inside the CESM1 Whole Atmosphere Community Climate Model version 4.0 (WACCM 4.0) (Garcia et al., 2007; Marsh et al., 2013) with Specified Dynamics (SD) coupled with the Community Aerosol and Radiation Model for Atmospheres (CARMA) model. The model is nudged with the Modern-Era Retrospective Analysis for Research and Applications (MERRA) (Kunz et al., 2011; Lamarque et al., 2012; Rienecker et al., 2011) for temperature, zonal and meridional winds, and surface pressure fields. This model has been used to simulate and analyze the PSCs during the Arctic winter of 2010–2011 (Zhu et al., 2015) and the Antarctic winter of 2010 (Zhu et al., 2017). The mesosphere/lower thermosphere Model for OZone And Related chemical Tracers (MOZART) in WACCM treats 18 PSC heterogeneous chemical reactions on aerosols and PSCs (Kinnison et al., 2007) and sulfur chemistry including reactions involving carbonyl sulfide, SO, SO_2, S, HSO_3, SO_3, and H_2SO_4 (English et al., 2011, and references therein).

In this paper, we improve this PSC model and compare simulations of both PSCs and related gas phase constituents with observations. Zhu et al. (2015, 2017) replaced the sulfate, STS, and NAT parameterizations in SD-WACCM (Kinnison et al., 2007; Wegner et al., 2013) with microphysical calculations. In this paper, we additionally replace the prognostic H_2O routines in SD-WACCM (Wegner et al., 2013) with microphysical calculations to treat ice cloud formation, dehydration, and conversions between ice and other PSCs (detailed below). Ice PSCs are only nucleated using CARMA when they are located between 90°S and 45°S latitude and at pressures less than 100 hPa. At pressures higher than 100 hPa the models' standard cloud parameterization is used to form tropospheric clouds including cirrus clouds. These parameterized clouds dehydrate the atmosphere and influence dynamics and radiative transfer, but they do not interact directly with nitric acid

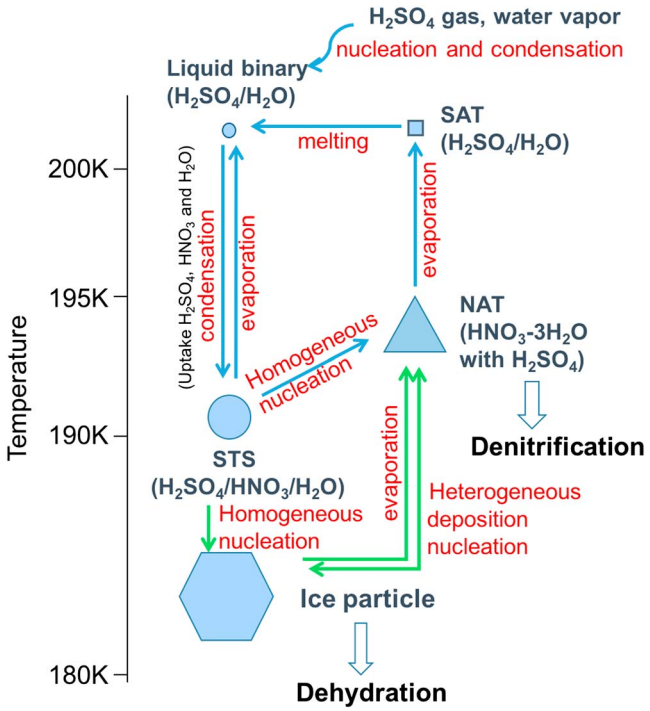

Figure 1. The PSC formation schemes in the current PSC model within the CARMA microphysical package. The liquid phase particles are symbolized as circles and solid phase particles as squares (SAT), triangles (NAT), and hexagons (ice). The hollow arrows indicate the main falling particles. The blue solid arrows are the processes described in Zhu et al. (2015); the green solid arrows are the processes we develop in this paper.

vapor or particles. Water vapor is exchanged with the standard WACCM model cloud scheme at the boundaries of this region. The time- and space-varying surface area density and effective radius of PSCs and sulfates determined by CARMA are passed into WACCM for heterogeneous reaction rate calculations.

The PSC tracers in the current model include 22 size bins for STS and NAT, which track varying compositions of H_2SO_4 and HNO_3 as also included in the previous model version (Zhu et al., 2015, 2017). The current model also includes 22 size bins for ice which track different amount of H_2SO_4, HNO_3, and H_2O inside ice. The particle sizes of all particle bins vary from approximately 0.3 nm to 20 μm with a volume ratio of 5.76 between bins. Particulate water is assumed to stay in equilibrium with the gas phase for STS and NAT particles, while it is treated explicitly in ice particles.

Figure 1 outlines the PSC microphysical processes treated in the current CARMA model. The blue solid arrows indicate the microphysical process for sulfate aerosols (English et al., 2011) and STS and NAT formation (Zhu et al., 2015). The green solid arrows indicate the microphysical processes for ice nucleation and growth as well as ice evaporation.

3.1. Microphysical Process Description

The microphysical processes and equations for type I PSCs (STS and NAT) in our model are detailed in Zhu et al. (2015). Below we describe the microphysical approaches used for ice PSCs.

3.1.1. Homogeneous Nucleation

Ice particles can form by homogeneous nucleation of ice in STS. We use the theory of homogeneous nucleation from Koop et al. (2000). The nucleation probability describes the fraction of STS particles of volume V that nucleate to form ice within a time step, t:

$$Probability_{homnuc} = 1 - \exp(-J_{homnuc} V t)$$

The theory calculates the volume nucleation rate coefficient:

$$J_{homnuc} = \exp\left(-906.7 + 8502\Delta a_w - 26924(\Delta a_w)^2 + 29180(\Delta a_w)^3\right)$$

where Δa_w is defined as the "water activity criterion" for homogeneous ice nucleation, which is an offset between the water activity of an aqueous solution for the ambient temperature and atmospheric pressure and the water activity of a solution in equilibrium with ice under ambient temperature (Koop et al., 2000). Here the water activity of the solution is the ratio between the water vapor pressure of STS and of pure water under the same conditions. The water vapor pressure of STS is calculated from Luo et al. (1995).

3.1.2. Heterogeneous Nucleation

The other way to form ice particles is from heterogeneous nucleation of ice on NAT. Here we use the classical theory of heterogeneous nucleation of ice (Pruppacher & Klett, 1997; Toon et al., 1989). The nucleation probability of ice particles on NAT within a time step, t, is expressed as

$$Probability_{hetnuc} = 1 - \exp(-J_{hetnuc} t)$$

The nucleation rate is expressed as

$$J_{hetnuc} = C_m n_\infty r^2 \left(\frac{2\sigma M_w}{A\pi\rho_i^2}\right)^{\frac{1}{2}} \exp\left(-\frac{4\pi\sigma a^2 f}{3kT}\right)$$

where T is the temperature in Kelvin; k is the Boltzmann constant (1.38054×10^{-16} erg/K); C_m, the number of H_2O molecules absorbed on the surface of the particles per unit area, is assumed to be 3×10^{15} cm^{-2}, which is a typical absorbed surface coverage (Toon et al., 1989); n_∞ is the number density of H_2O molecules in the gas phase with the unit of cm^{-3}; r is the radius of the NAT particle with the unit of cm; σ is the surface tension

of ice which equals to $(141 - 0.15T)(1 + \gamma/r)$ erg/cm^2, where γ is 3×10^{-8} cm; M_w is the molecular weight of water (18.02 g/mol); and ρ_i is the particle density of ice, which is assumed to be 0.9 g/cm^3. The radius of the germ (a) is expressed as

$$a = \frac{2M_w\sigma}{RT\rho_i \ln(S)}$$

where R is the gas constant (8.31430×10^7 erg/K/mol) and S is the saturation ratio of H_2O with respect to a plane ice surface. The factor f represents the lowered surface energy associated with the curvature of the heterogeneous nucleus surface relative to nucleation from the vapor. It is expressed as

$$f = 0.5\left\{1 + \left(\frac{1 - mx}{\phi}\right)^3 + x^3\left[2 - 3\left(\frac{x - m}{\phi}\right) + \left(\frac{x - m}{\phi}\right)^3\right] + 3mx^2\left[\frac{x - m}{\phi} - 1\right]\right\}$$

where

$$x = r/a; \quad \phi = \left(1 - 2mx + x^2\right)^{1/2}$$

Here m is a factor related to the energy barrier for particle nucleation. For NAT particles, we assume m= 0.95 based on the calculation by Toon et al. (1989).

3.1.3. Growth and Evaporation

The growth and evaporation of ice particles follows Toon et al. (1989) and Zhu et al. (2015), who discuss the parameters in the equations we use for PSC model. We ignore the effects of solutes such as HCl on the vapor pressure and we ignore radiative heating of the particles. The vapor pressure over ice in pascal as a function of temperature (Murphy & Koop, 2005) is

$$p_{ice} = \exp\left(9.550426 - \frac{5723.265}{T} + 3.53068\ln(T) - 0.00728332T\right); \quad T > 110K$$

We also assume that nitric acid vapor and sulfuric acid vapor contribute to the growth and evaporation of the ice particles. These materials are kept track of within the ice particles, along with the nitric acid and sulfuric acid that may have been in the original nuclei.

3.1.4. Sublimation

As ice particles evaporate, the H_2O in the ice goes directly to the gas phase until the NAT/SAT that was in the ice particle is left behind as an independent particle.

3.1.5. Coagulation

Coagulation is not an important process for ice particles in PSCs since the number density of ice particles is small and the lifetime of ice particles is short. We do consider the coagulation of sulfuric acid particles with each other since they may have large number densities due to nucleation from the vapor.

3.2. Gravity Waves Over the Antarctic Mountains

Gravity wave activity can be simulated by high-resolution models, but we must parameterize them. We follow the criteria described in Alexander et al. (2013) to determine when mountain waves are present above the larger Antarctic mountain ranges. For mountain waves to be present, the horizontal wind speed V_H at 800 hPa must exceed a threshold 10 m/s; the wind direction θ at 800 hPa must be within a specific range of angles near 45° from the normal of the mountain range. Waves are assumed to form up to the altitude at which the wind turning angle $\delta\theta$ from lower troposphere to the grid cell in question is larger than 45°. Here we use the model winds nudged to MERRA wind data to determine the propagation of gravity waves into stratosphere. For each grid point in one model time step which is orographic gravity wave active, we choose a random number between +2 K and −2 K as the temperature fluctuation and apply it to the CARMA microphysics package at that grid point and time step without influencing either the dynamic or chemistry packages. We also conduct test cases with larger (±3 K, ±4 K) and smaller (±1 K) temperature fluctuation. Because these results are qualitatively similar to the 2 K case and to limit the total number of figures in the paper, we do not show the figures from these cases but their results will be discussed below. Waves do not propagate between time steps nor do they have any vertical structure, since each grid cell is given a random temperature perturbation. Figure 2 shows an example of the locations and the percentage of days with orographic gravity waves in the Antarctic stratosphere at 52 hPa in the 2010 Antarctic winter. The major wave

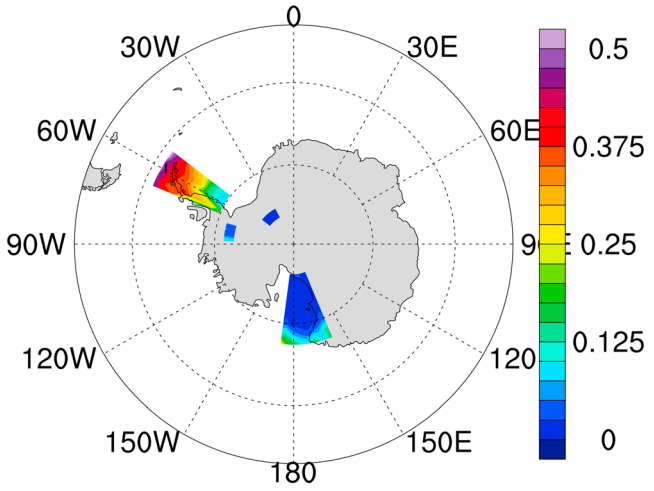

Figure 2. The percentage of days with orographic gravity waves over Antarctica at 52 hPa from 1 May to 30 October 2010.

areas are over the Antarctic Peninsula, where some regions have orographic gravity waves ~50% of the time, and over the Ross Ice Sheet.

4. Simulation From 2010 Antarctic Winter

4.1. Cases Considered

We conduct simulations for 2010 Antarctic winter from 1 May to 31 October. The model has a horizontal resolution of 1.9° in latitude and 2.5° in longitude and 88 pressure levels from the surface to 6×10^{-6} hPa (about 140 km). For the stratosphere, the vertical resolution is about 1 km. We examine two simulations using the SD-WACCM/CARMA model. The first case, which we call the base case, uses the full PSC model described in Figure 1, but does not have any gravity wave perturbations to the temperature field. The second simulation, which we call the wave case, applies random temperature fluctuations to the base case temperature fields for the microphysical processes when the gravity wave criteria are met over the Antarctic mountains as described in section 3.2. One of the purposes for our WACCM/CARMA simulations is to give improvement suggestions for the WACCM PSC parameterizations. Therefore, we compare our simulations with a case using SD-WACCM with the standard PSC parameterizations in MOZART (called the WACCM case). The WACCM case is from the Standard Chemistry-Climate Model Initiative REF-C1 simulation with the Trop-Strat-Meso-Lower Thermosphere MOZART chemistry. The standard PSC scheme uses prescribed supersaturations, size distributions, and number densities for STS and NAT (Kinnison et al., 2007; Wegner et al., 2013) and uses a prognostic H_2O routine to treat ice cloud formation and dehydration (Wegner et al., 2013).

4.2. Size Distribution

The size distribution of PSC particles influences dehydration, denitrification, surface area density, and the radiative effects from PSCs. Our microphysical model is able to track the size and number of aerosols and PSCs instead of using fixed size distributions assumed in many climate models, such as WACCM's original PSC parameterization. Zhu et al. (2015) showed the WACCM/CARMA model simulates the observed STS size distribution within error bars. The PSC model (Zhu et al., 2015, 2017) with homogenous nucleation of NAT from STS creates particles with radii that are often larger than 10 μm. Such large particles are needed to reproduce the observed denitrification. However, the backscattering ratio from CALIPSO in the Antarctic midseason shows large backscattering ratios from NAT/STS mixtures, which indicates a higher number density and smaller size of NAT than are produced by the model without ice particle physics (Zhu et al., 2017).

Figure 3 shows the HNO_3 mixing ratio in NAT, NAT effective radius, and NAT effective radius probability distribution function from the base case simulation, which has no mountain waves. We compare the results from 27 May, 10 July, 16 July, and 24 July to analyze various NAT particle sizes with and without ice formation in previous days. As discussed by Zhu et al. (2017) these days are representative of different NAT forming mechanisms. On 27 May, at the beginning of the winter, ice rarely forms. These NAT particles are nucleated from STS through homogeneous nucleation and have a radius around 10 μm. On 10 and 16 July, we see a bimodal distribution of NAT with one mode covering from submicrometer (i.e., smaller than 1 μm) to ~2 μm, and another mode ~8 μm. We find that STS forms near the Antarctic Peninsula and ice forms near the pole and the Antarctic Peninsula during the previous days for these two dates. The coexistence of STS and ice clouds results in the production of both large and small NAT particles. On 24 July, NAT particles are produced by ice evaporating downwind of the Antarctic Peninsula in the previous days. During these days, STS rarely forms, and therefore, there are no large NAT particles on 24 July. These NAT particles cover a wide size range with radii from submicrometer to ~4 μm. Therefore, it is very important to include both homogeneous nucleation from STS and heterogeneous nucleation from ice in the model, in order to simulate both large and small NAT particles.

Gravity waves produce ice clouds with large number densities of particles. Figure 4 shows the number density of NAT and ice when we introduce mountain waves as described in section 4.1 (the wave case). The ice and NAT number densities increase about 1 order of magnitude compared with the base case on 20 July at 52 hPa.

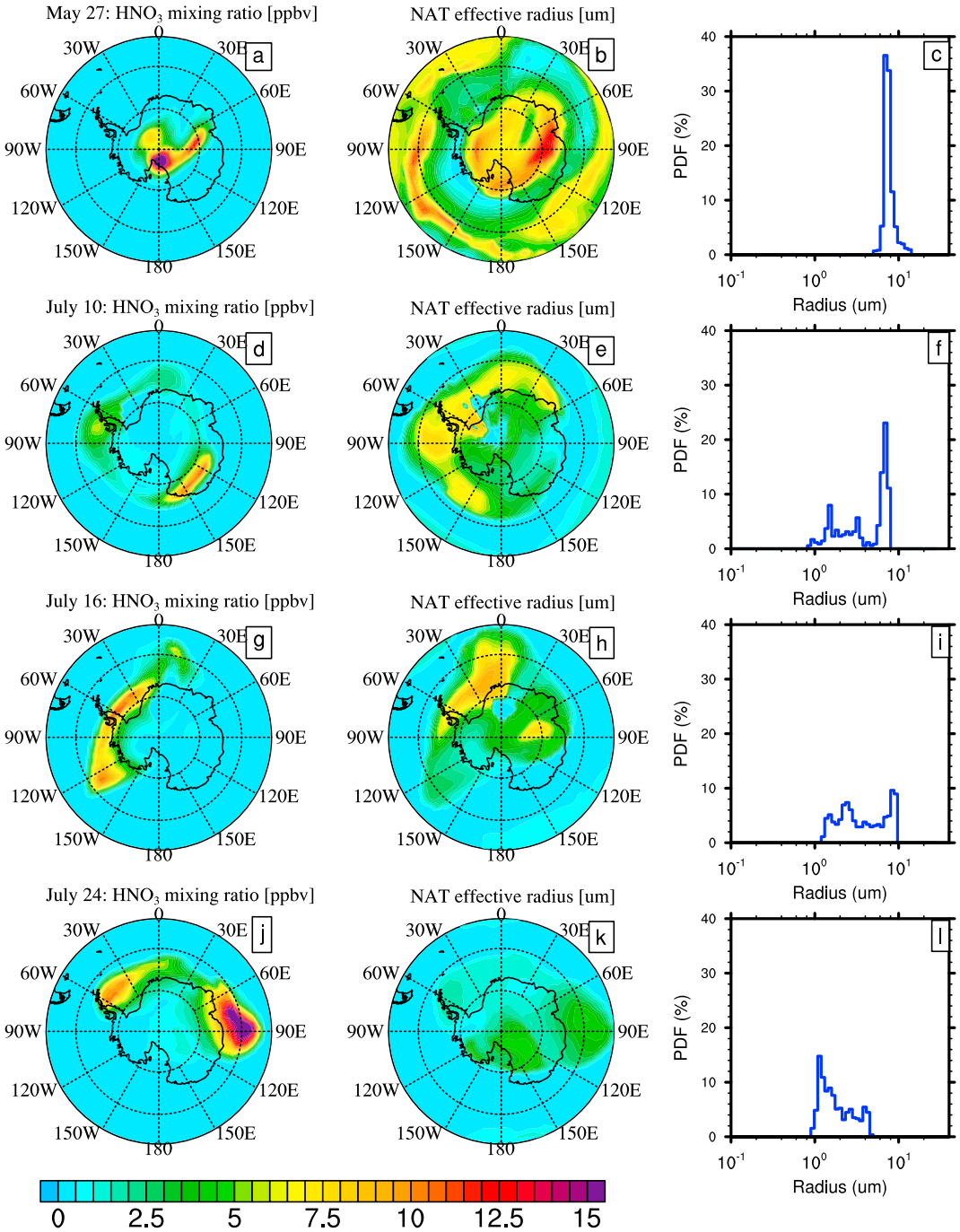

Figure 3. (a–l) The simulated HNO_3 mixing ratio in NAT, NAT effective radius, and NAT effective radius probability distribution function (PDF) at 52 hPa on 27 May, 10 July, 16 July, and 24 July 2010. The PDF for the effective radius of NAT is calculated where the HNO_3 mixing ratio in NAT is higher than 2 ppbm inside the vortex.

4.3. Simulated PSC Optical Properties Compared With CALIPSO Observations and Simulated Nitric Acid and Water Compared With MLS Observations in Early Winter and Midwinter

The CALIPSO satellite observes backscatter and polarization of light from clouds and aerosols. The CALIPSO team developed a detection algorithm for the PSC optical properties and defines PSCs in up to six categories as we describe in section 2.1 (Pitts et al., 2007, 2009). Here we compute the optical properties from the simulation to compare with CALIPSO data using a T matrix approach (Mishchenko & Travis, 1998) with real refractive indices of 1.43 for STS, 1.50 for NAT, and 1.308 for ice (Pitts et al., 2009). We

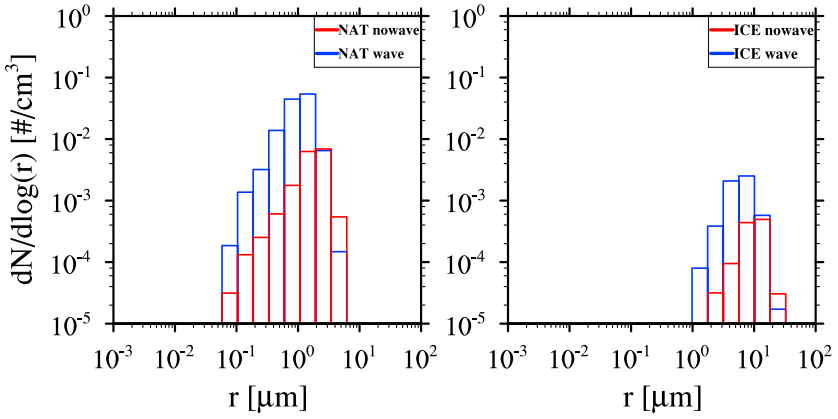

Figure 4. The number size distribution of NAT and ice on 20 July 2010 at 52 hPa inside the vortex with and without waves.

assume NAT and ice to be spheroids with an aspect ratio of 0.9 and 0.95 and STS to be spherical. The reasons for these parameter choices are given in Zhu et al. (2017). We consider the mixing of PSC types in two ways. First, we consider all types of PSCs in one grid box as one mixed PSC cloud and calculate its backscatter and depolarization. In this case we cannot uniquely identify the optical properties with a simulated PSC composition. We define the PSCs the same way as CALIPSO does. Second, we consider PSCs in one grid box as separate PSC clouds by composition and calculate the backscatter and depolarization individually. In this case we can uniquely identify the composition and related optical properties. The simulations do not have noise, which is intrinsic to CALIPSO, in the optical parameters. We have added noise to the simulated backscatter and depolarization as described in Engel et al. (2013).

PSCs start to form at the end of May. Figure 5 shows the backscatter and depolarization features from the PSCs from 24 to 28 May at 52 hPa in the base case. Both the CALIPSO observations and the simulations show a large amount of STS with backscattering ratio as large as 5, while the majority of the particles with a nonzero depolarization ratio are located in Mix1 and Mix2 categories. However, CALIPSO observes a small number of particles with large backscattering ratio as well as large depolarization, which are classified in Mix2-enhanced and ice categories, while the model does not reproduce this feature. When we compare the same data in a polar view (Figure 6), the simulations show that STS

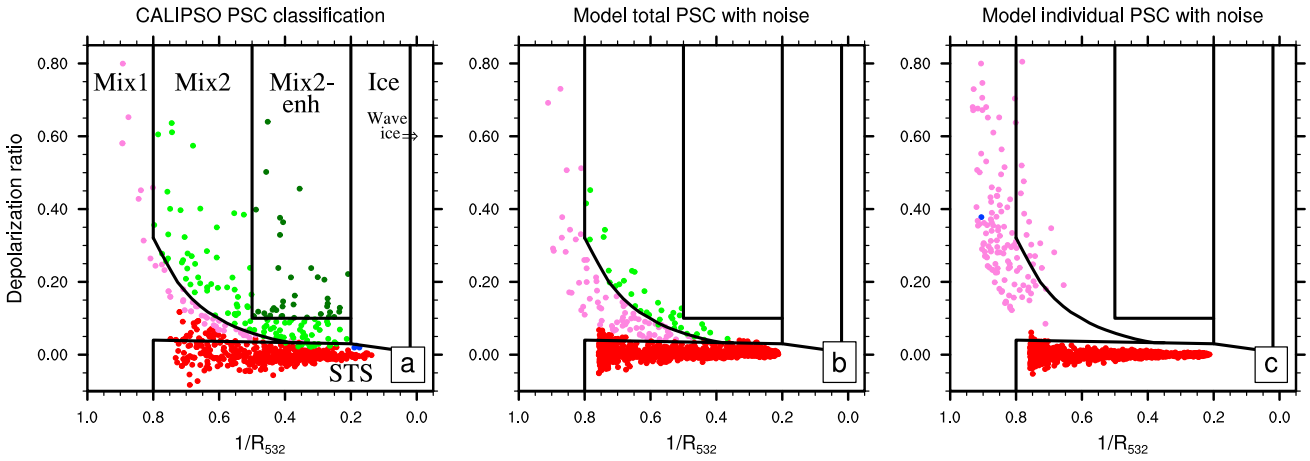

Figure 5. CALIPSO PSC classification compared with model derived classification from 24 to 28 May 2010 at 52 hPa. (a) The CALIPSO algorithm defined STS class is in red, the Mix1 class in purple, the Mix2 class in green, the Mix2-enhanced class in dark green, and the ice class in blue. (b) The modeled total PSC backscatter versus depolarization follows the same definitions and colors as the CALIPSO algorithm. (c) The modeled individual PSC groups are shown. The STS is shown in red and the NAT is shown in purple. No ice is present. The red dots include clouds with $R_{532} > 1.32$ and perpendicular backscatter coefficient $<3.28 \times 10^{-6}$ km^{-1} sr^{-1}, indicating that STS is present in regions outside the CALIPSO classification boundary.

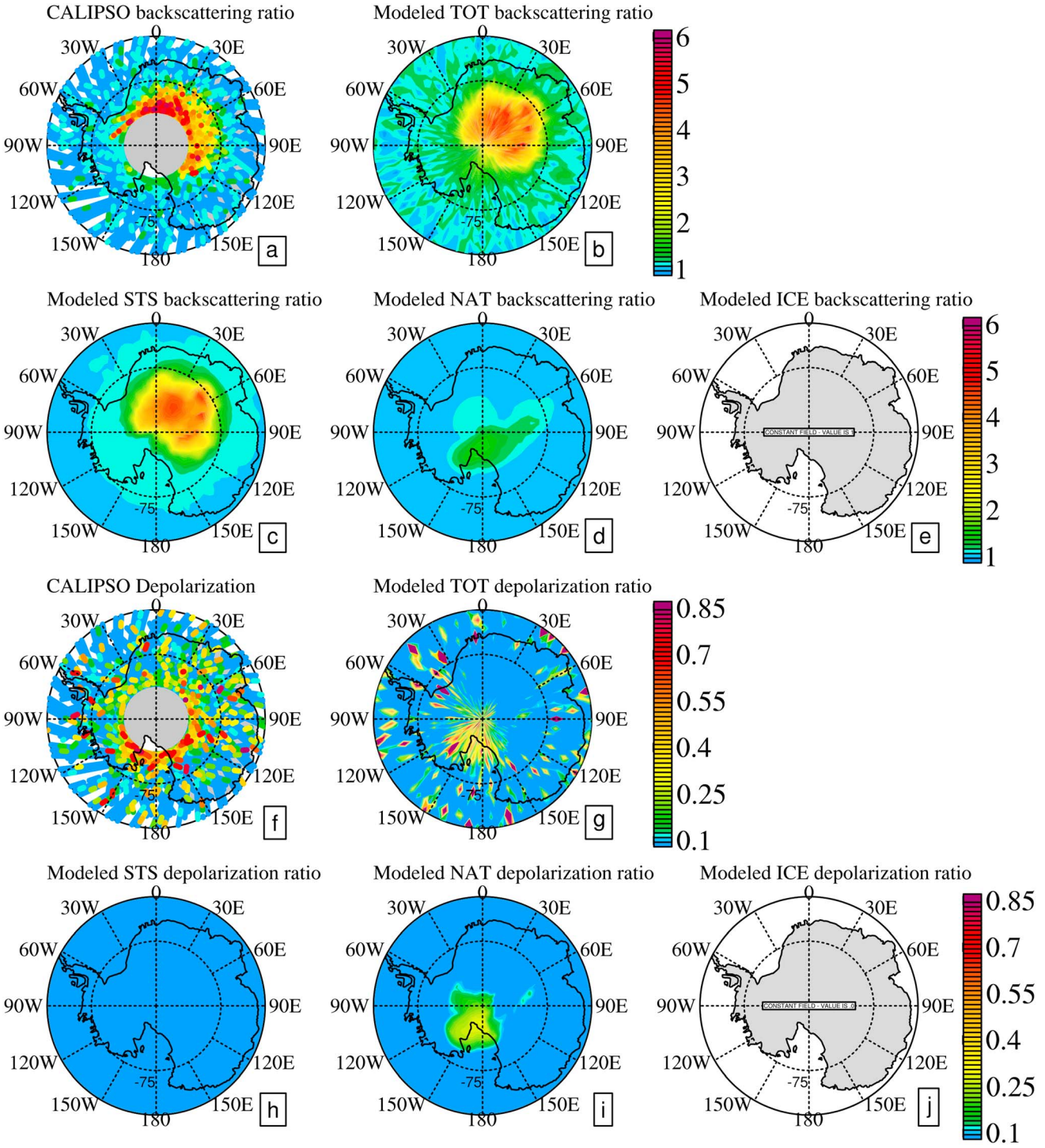

Figure 6. The CALIPSO and simulated PSC properties at 52 hPa from 24 to 28 May 2010. (a–e) The maximum CALIPSO backscattering ratio compared with the modeled maximum backscattering ratio. We compute the maximum backscatter for the comparison partly because the CALIPSO footprints often overlap especially in the area close to the pole. When two points overlap, we plot the point with the larger number. Further from the pole the CALIPSO points diverge so at sometimes there are no measurements. By using the maximum value we avoid averaging in points with no data. Likewise for the model we plot the largest value during the period. (f–j) The maximum CALIPSO depolarization ratio compared with the modeled maximum depolarization ratio. The noise is only added to modeled total backscattering ratio (Figure 6b) and modeled total depolarization ratio (Figure 6g).

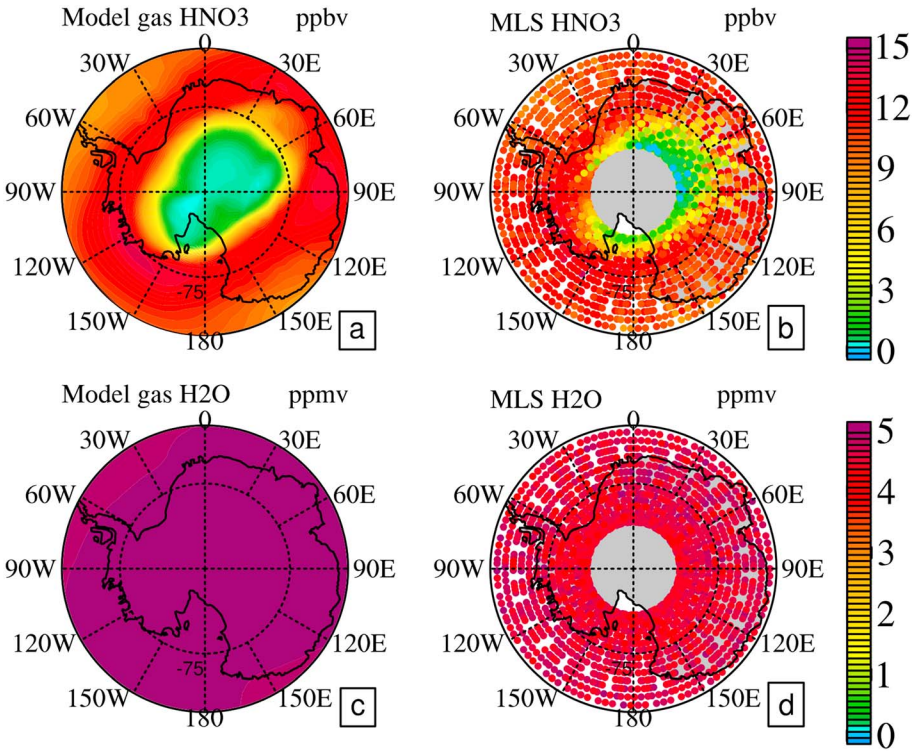

Figure 7. The modeled average (a) HNO_3 and (c) H_2O compared with the (b) MLS HNO_3 and (d) H_2O at 52 hPa from 24 to 28 May 2010.

provides most of the backscatter and is mainly located over East Antarctic. The simulated NAT has a small backscattering ratio (~1.5) and a strong depolarization poleward of the Ross Ice Sheet, which is consistent with locations at which CALIPSO observes high depolarization. The CALIPSO classification indicates many places with mixed STS/NAT particles from 0°E to 90°E but the simulation does not produce NAT in most of this sector. The CALIPSO classification also indicates a small amount of ice. In the previous work done by Zhu et al. (2017), the same temperature fields were used as in the runs presented here. In the older model, ice which was parameterized to form based on humidity provided most of the backscattering ratio rather than STS. The ice also provided large depolarization in East Antarctica. The current model, by considering ice nucleation from STS and NAT, does not produce ice in late May either in the base case (Figure 6) or in the wave case (not shown). The observed ice and NAT/STS mixtures in Mix2-enhanced categories are mainly located over East Antarctica from 0°E to 120°E. The lack of these clouds in the model might be caused by several factors we have not considered during the simulation: larger-amplitude temperature fluctuation from mountain waves than the 2 K assumed, general unresolved background temperature fluctuations (Podglajen et al., 2016), or nonorographic inertial gravity waves which have been observed to be responsible for ice PSCs in Antarctica (Shibata et al., 2003). Engel et al. (2013) also shows the importance of including small-scale background temperature fluctuations in order to reproduce the large ice PSC backscattering ratio as seen by CALIPSO.

The simulated HNO_3 vapor shown in Figure 7 indicates that the temporary denitrification area near the pole in the model is close to the one observed by MLS. However, MLS cannot observe the area south of 82°S. There is no temporary dehydration in either the MLS observations or the simulations, but the model has about 1 ppm more water than observed probably because the initial H_2O condition in the model is slightly higher than MLS observations.

On 18–22 July, CALIPSO (Figure 8a) observed STS with large backscattering ratio (>2.5) and particles classified in ice categories, while the modeled cases with or without wave do not show particles in the CALIPSO ice category, though ice is present in the simulation (the blue dots in Figures 8d and 8e). This difference

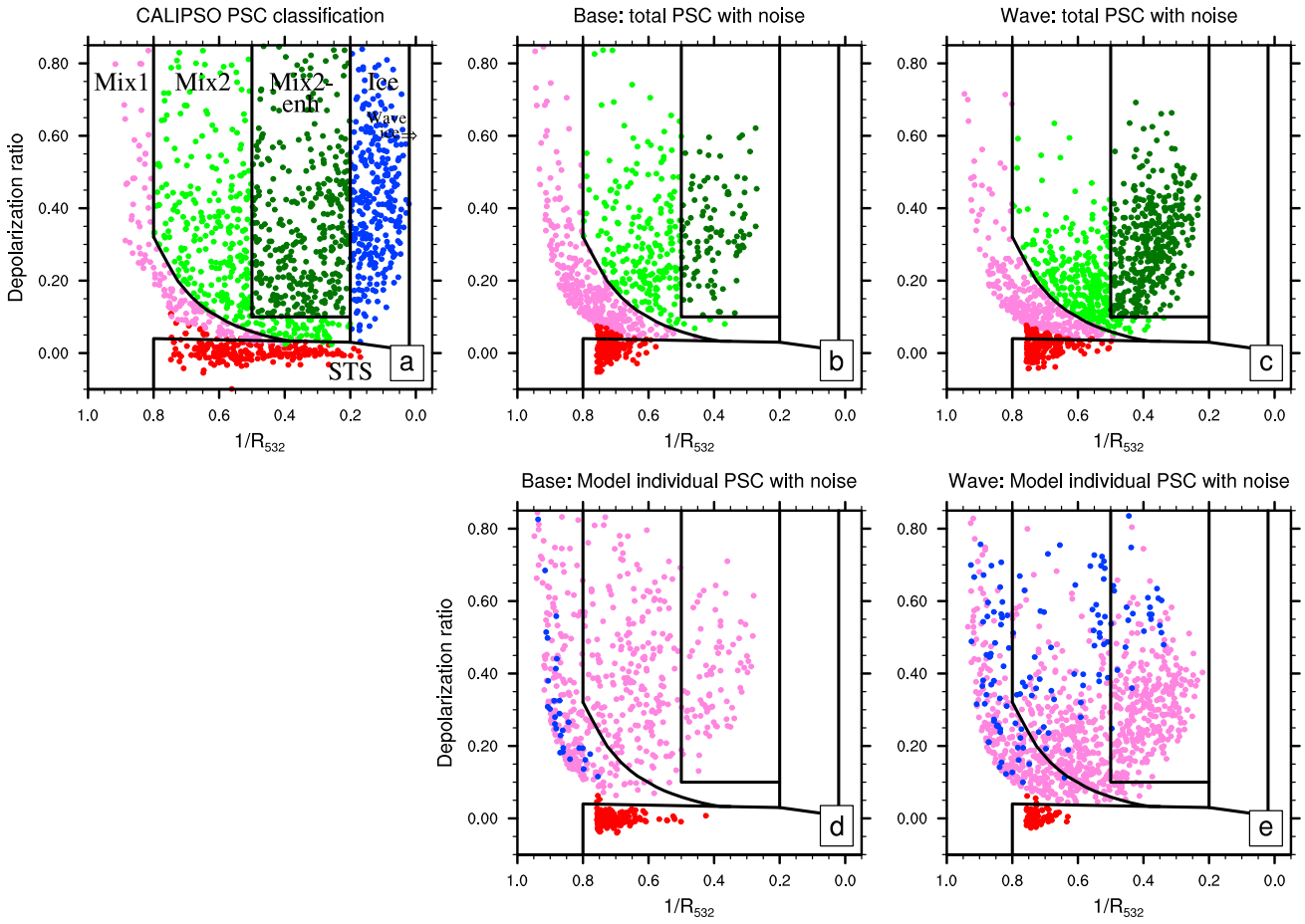

Figure 8. CALIPSO PSC classification compared with modeled two cases' derived classifications from 18 to 22 July 2010 at 52 hPa. The STS is shown in red, the NAT is shown in purple, and the ice is shown in blue.

may be because the denitrification and dehydration in the Antarctic midseason causes the STS/ice mixtures to have a backscattering ratio that is lower than the ice class boundary (Pitts et al., 2013; Zhu et al., 2017). Or it may be that higher-amplitude mountain waves are present than assumed in the simulations or that background gravity waves, which are not included in the simulations, are important. Comparing the base case (Figure 8b) and the wave case (Figure 8c), the wave case has more particles in Mix2 and Mix2-enhanced categories. The simulated individual PSCs (Figures 8d and 8e) show more NAT and ice particles with higher backscattering ratio in the wave case.

In Figure 9, the base case shows a slightly higher backscatter due to STS and a slightly lower backscatter due to ice compared with the wave case. Also, because of the increasing number density of ice and NAT due to gravity waves, it also shows a higher backscattering ratio from NAT in the wave case than in the base case. In test cases (not shown here), decreasing the amplitude of temperature fluctuations to ±1 K decreases the backscattering ratio from NAT and ice particles, whereas increasing the amplitude to ±3 K and ±4 K increases the NAT and ice backscattering ratio. A small amount of the ice mixtures with backscattering ratio higher than 5 are produced in ±4 K case (not shown here); however, the CALIPSO observation shows a backscattering ratio of about 6, downwind of the Antarctic Peninsula. None of our simulations reproduce a backscattering ratio as high as the observation. It is likely that a more complete wave model is needed to better simulate the CALIPSO data. Or the irreversible denitrification earlier in the season in our model is too strong so that the nitric acid in the condensed phase is not enough to form the right amount of PSCs in the midseason. Compared with CALIPSO observation, the NAT particles in Figure 9 show strong backscatter at 10°W–30°W, north of 60°S. Since the gas phase HNO_3 is close to the observation, the partitioning of large NAT particles and small NAT particles in the model may not

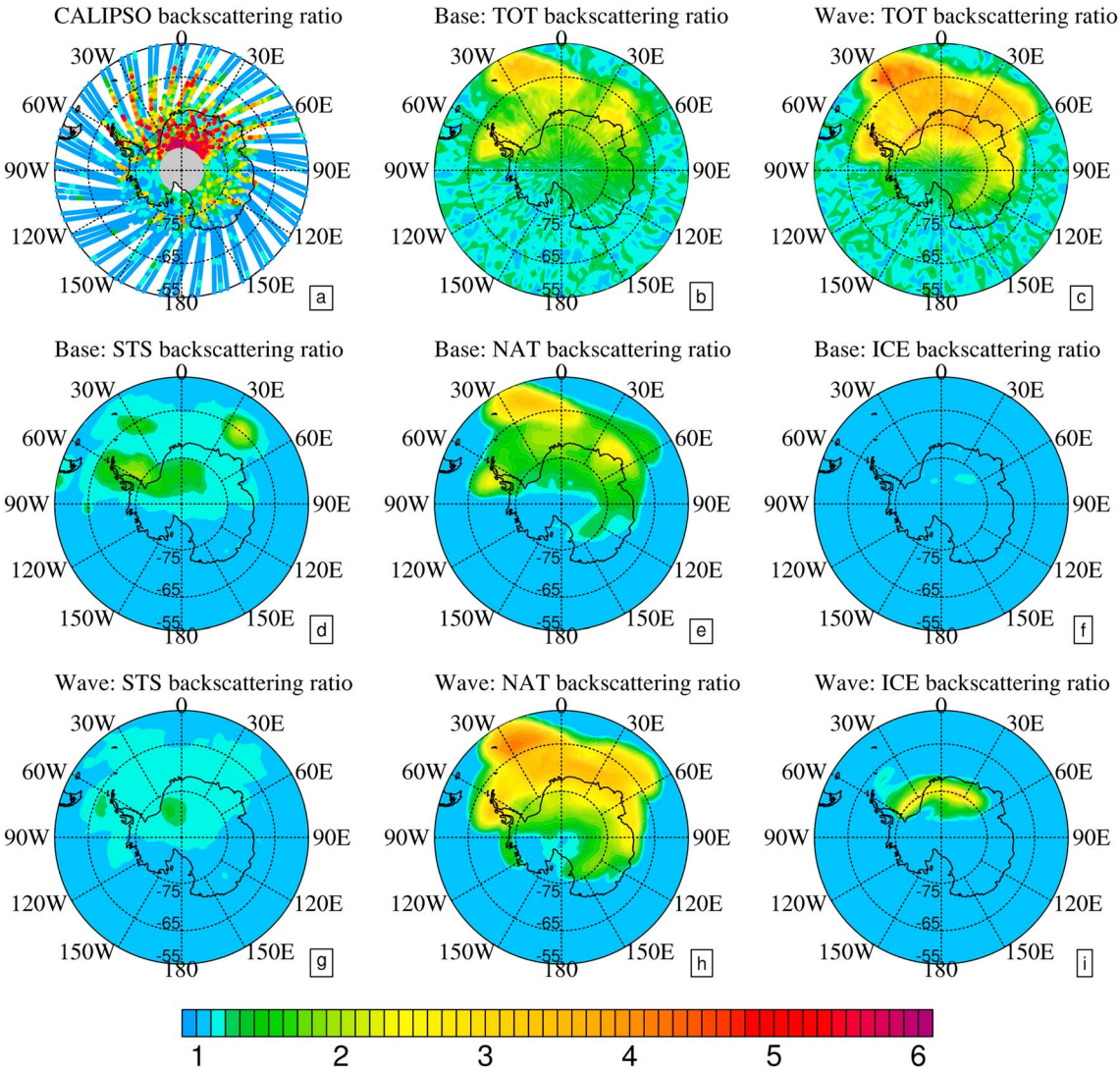

Figure 9. The PSC backscattering ratio at 52 hPa from 18 to 22 July 2010. (a–c) The maximum CALIPSO backscattering ratio compared with the modeled maximum total backscattering ratio from base and wave cases. (d–f) The maximum backscattering ratio for STS, NAT, and ice, respectively, from the base case. (g–i) The maximum backscattering ratio for STS, NAT, and ice, respectively, from the wave case. The noise is only added to modeled total backscattering ratio (Figures 9b and 9c).

be consistent with nature. In the previous model version (Zhu et al., 2017) when the model does not form small NAT particles, there is rarely any backscatter in this area. Figure 10 shows that the modeled NAT contributes to most of the depolarization. Ice in the wave case also contributes some downwind of the Antarctic Peninsula. Both the base case and the wave cases show similar patterns and amount of gas phase HNO_3 (Figures 11a–11c), total (sum of gas and particle phase) HNO_3 (Figures 11d and 11e), and gas phase H_2O (Figure 12). The temporary denitrification in the simulated cases (Figures 11b and 11c) covers a slightly larger area than the MLS shows (Figure 11a). The modeled water vapor is similar to the MLS observation (Figure 12).

Because of the possible deficiency of temperature perturbation representations in the model, we provide a further analysis of the model temperature. Figure 13 shows the gravity wave percentage and minimum temperature over the Antarctic Peninsula during 21 to 28 May and 15 to 22 July 2010. During 21 to 28 May, gravity waves are relatively active from 22 to 24 May and provide a slightly lower temperature in the wave case. However, the minimum temperatures over the Antarctic Peninsula in this period are all above ice frost point (~188 K), so the gravity wave with the assumed amplitude cannot trigger ice formation. During 15 to 22 July, gravity waves are active on 15, 16, and 18 July and the minimum temperatures

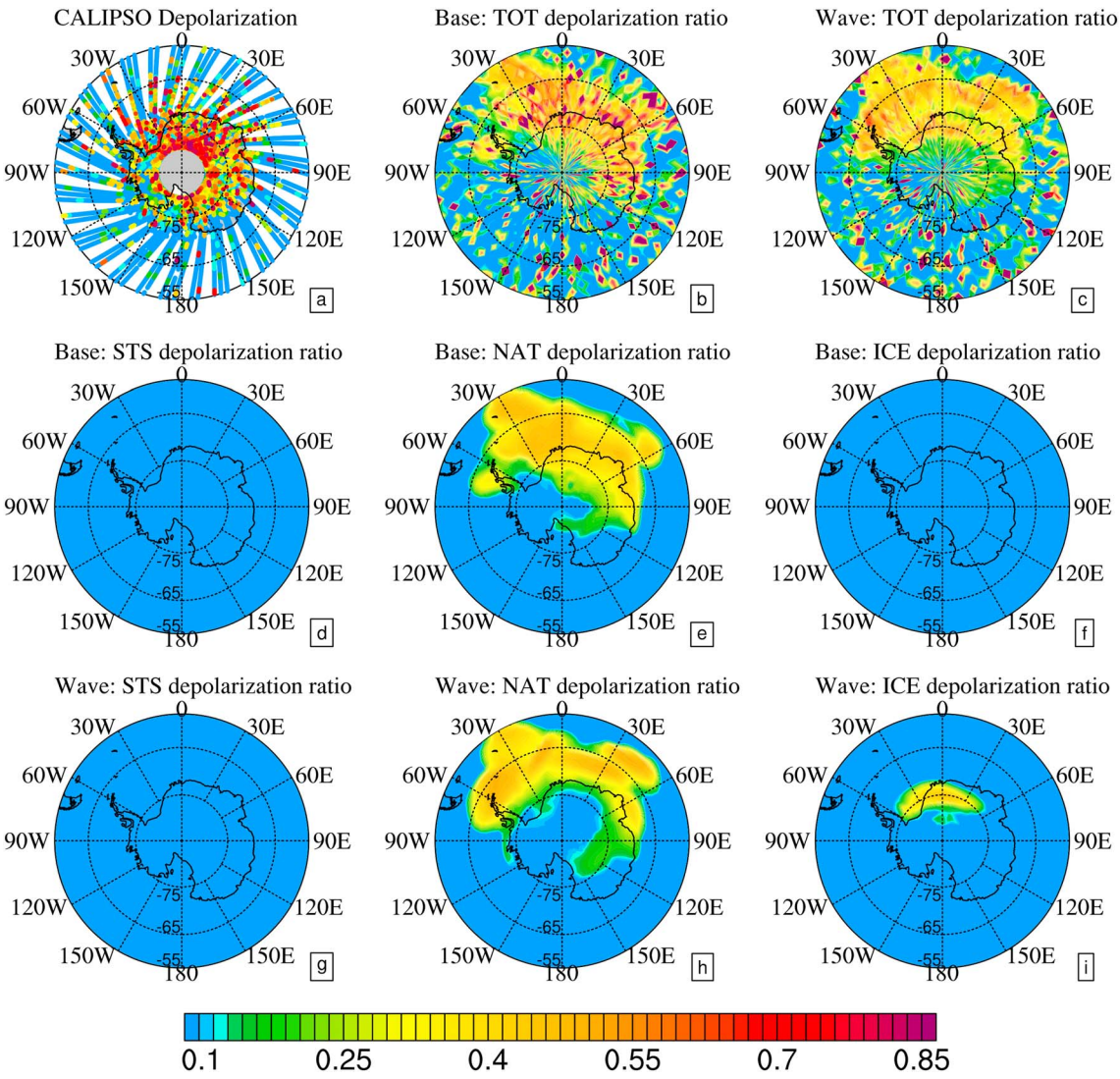

Figure 10. (a–i) The CALIPSO and simulated PSC maximum depolarization at 52 hPa from 18 to 22 July 2010. The orders of the figures are the same as in Figure 9.

are below ice frost point during 17 to 20 July. Therefore, on these days the gravity waves over the Antarctic Peninsula provide important temperature perturbations to trigger the formation of large numbers of ice and NAT. We find that ERA-Interim reanalysis temperatures of European Centre for Medium-Range Weather Forecasts at these times at a higher, 0.75°, spatial distribution compared to our 1.9° are essentially identical to our temperatures, indicating that even higher-resolution models may needed to resolve the waves better.

4.4. Denitrification and Dehydration Throughout the Winter

The evolution of gases and particles in the lower stratosphere is not only influenced by PSC formation but also by atmospheric transport. Therefore, we compare the evolution of an inactive tracer species, N_2O, south of 80°S with MLS observations, and between 75°S and 80°S to evaluate the simulation of the descent of the air. Figure 14 shows the evolution of MLS N_2O compared with N_2O in the simulation. Referring to the pressure levels where PSCs often occur (from 20 hPa to 70 hPa), the N_2O descent from the simulations remain close to the MLS observations until the middle October, when the PSCs disappear and the vortex starts to break up. At that time, the model shows a significant increase of N_2O to over 50 ppbv between 21 hPa and 32 hPa, while the MLS N_2O remains below 50 ppbv. We conclude that the simulated descent is reasonable until mid-October.

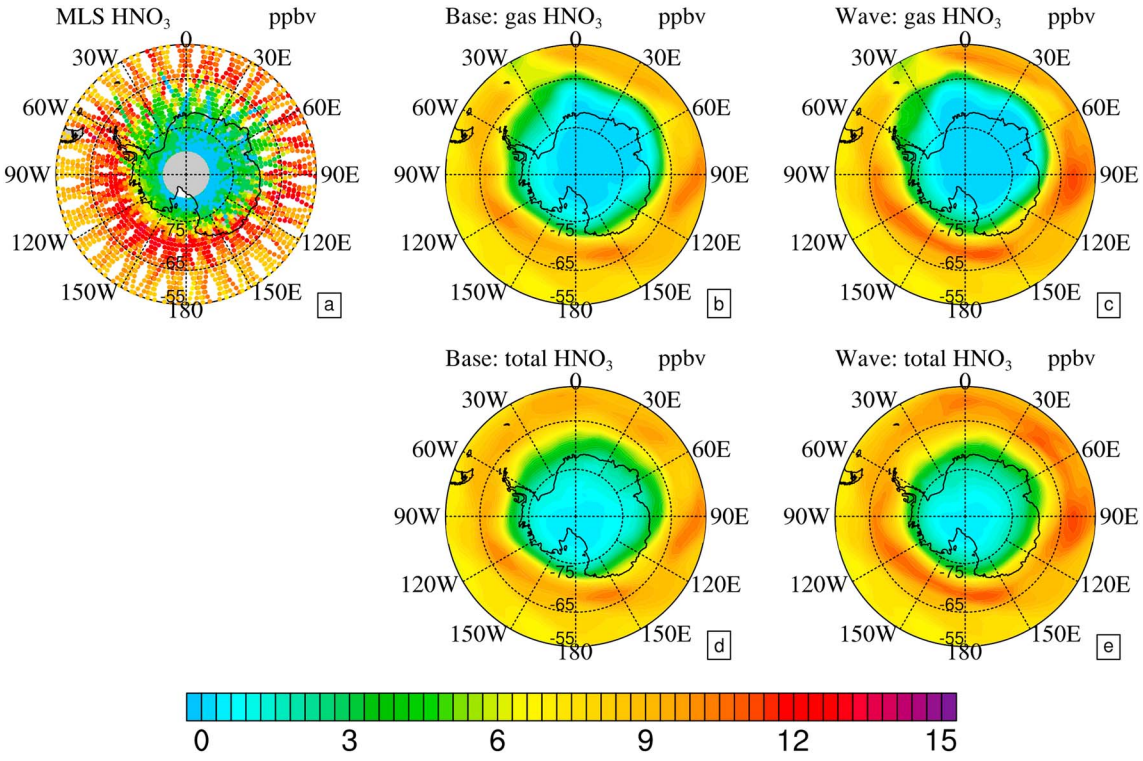

Figure 11. The HNO_3 at 52 hPa from 18 to 22 July 2010. (a–c) The MLS gas HNO_3 and modeled gas HNO_3 from the base case and the wave case. (e and f) The total HNO_3 from the base case and the wave case. The difference between the total and gas phase nitric acid is the particulate nitric acid.

Figure 15 shows the H_2O and HNO_3 evolution during the winter. The H_2O evolution for both the WACCM case and our model simulations are nearly within the error bars of the MLS observations. The WACCM case is slightly higher than the MLS observations at 68 hPa and 32 hPa. The base case and the wave case overlap with each other, which indicates that the waves do not influence the dehydration much. The HNO_3 evolution varies from case to case. The base case (without waves) is outside the error bars of the data most of the time except for the 68 hPa altitude level. The wave case almost overlaps with the base case except during August at 21 hPa. The temperature fluctuations due to the propagation of waves lead to more NAT particle formation at 21 hPa in August and causes lower HNO_3 amount. In test cases (not shown here), decreasing the amplitude of temperature fluctuations to ±1 K decreases the denitrification for 21 hPa, whereas increasing the amplitude to ±3 K and ±4 K increases

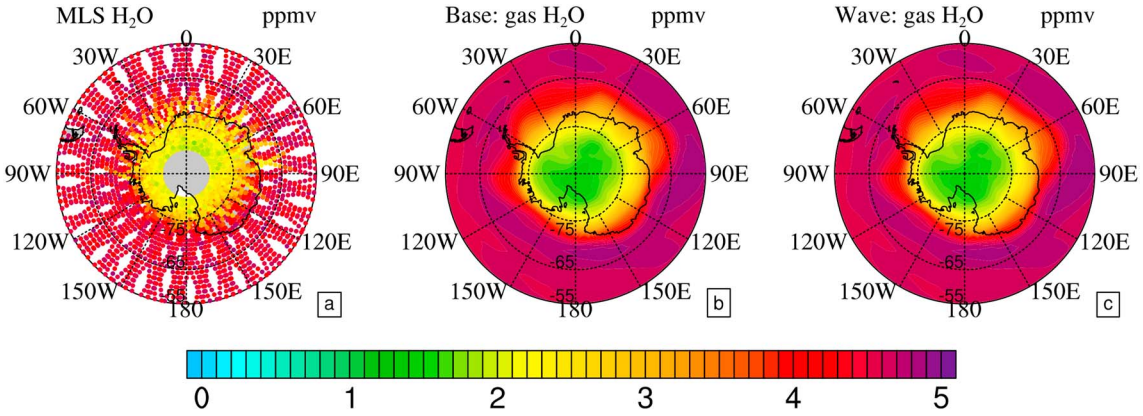

Figure 12. The (a) MLS and simulated average H_2O ((b) the base case and (c) the wave case) at 52 hPa from 18 to 22 July 2010.

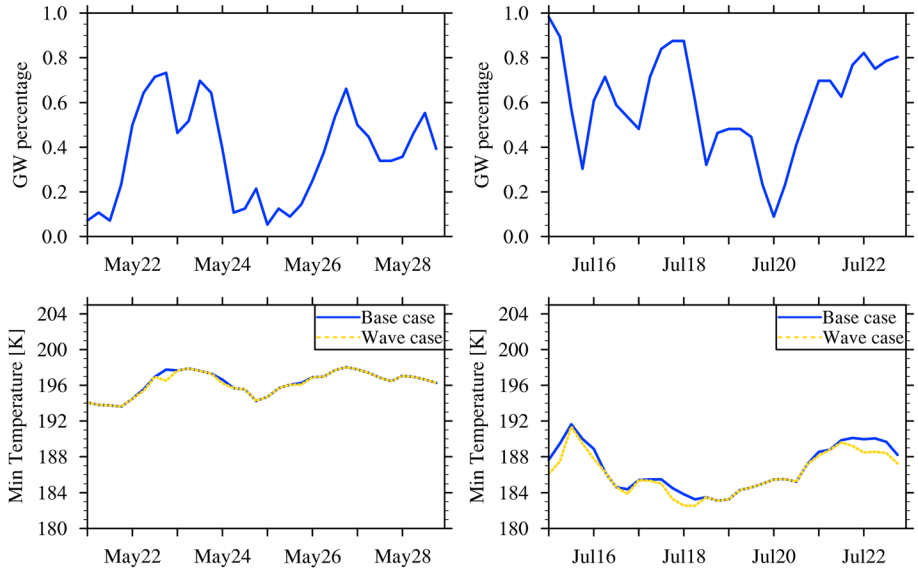

Figure 13. The gravity wave percentage and minimum temperature at 52 hPa over the Antarctic Peninsula before and during the two periods we have analyzed in section 4.3: 21 to 28 May and 15 to 22 July 2010. The gravity wave percentage is the number of grid boxes with gravity wave events at a specific time divided by the total number of grid boxes over the Antarctic Peninsula.

the denitrification. The HNO_3 in the WACCM case is higher than the observations at all levels. One possible explanation of the underestimation of denitrification in the WACCM case is that the number density and size distribution parameterizations are inappropriate. The number density of NAT is assumed to be 10^{-2} cm^3, and the calculated size of NAT is generally smaller than 2 μm. It is important to include

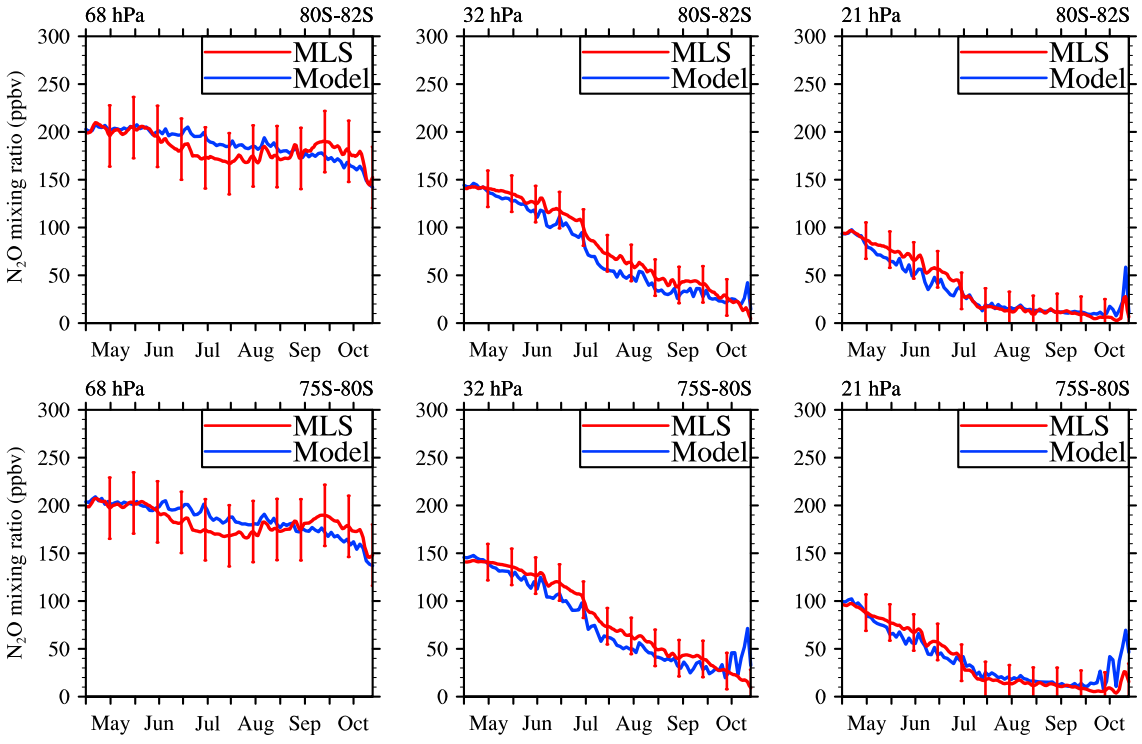

Figure 14. The evolution of N_2O mixing ratio throughout the 2010 Antarctic winter and spring from MLS observation (red) with error bars (Livesey et al., 2011) and the model (blue) at different pressure levels.

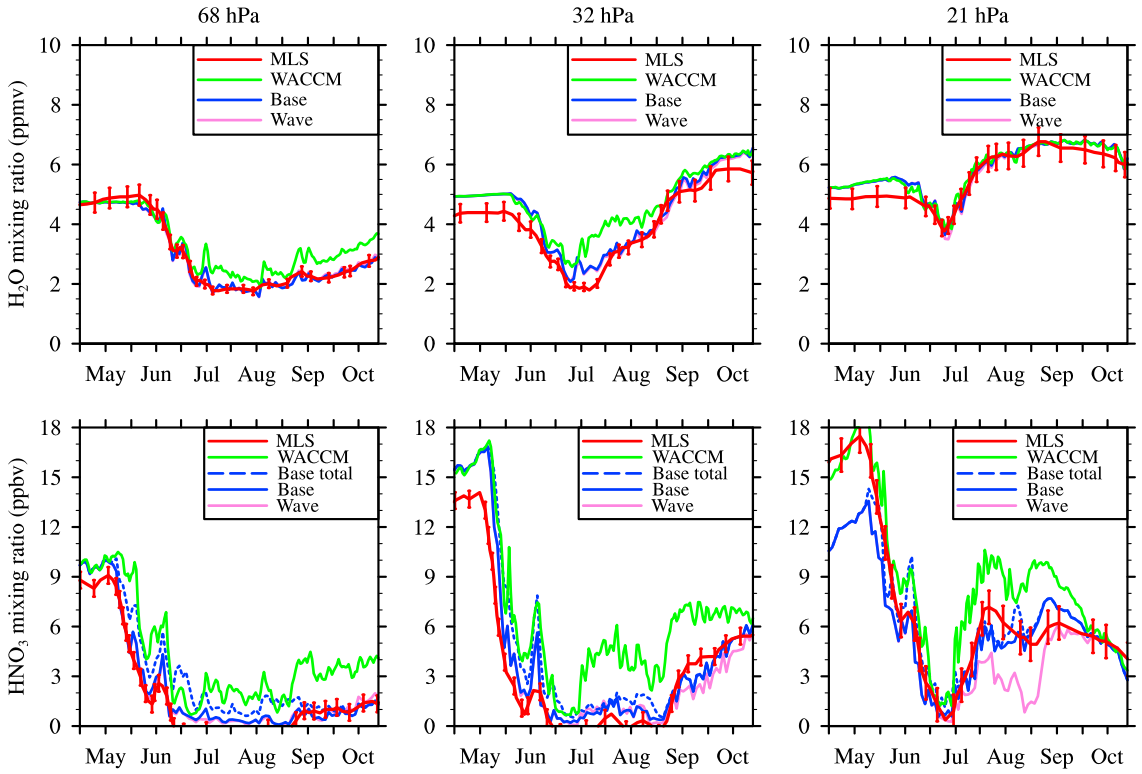

Figure 15. The H_2O and HNO_3 evolution at different pressure levels during 2010 Antarctic winter. Shown are the 80°S–82°S average values. The red line is the MLS observation (de Laat & van Weele, 2011) with error bars (Livesey et al., 2011). The blue and purple lines are from our two simulation cases without and with the gravity waves. The dashed blue line is the total HNO_3 in the base case, indicating the irreversible denitrification. The green line is from the WACCM case with standard PSC parameterizations.

large NAT particles, even with small number densities, in the model in order to correctly simulate the denitrification. We suggest that the WACCM/MOZART PSC parameterization should assume a bimodal size distribution of NAT particles. Solomon et al. (2015), for 2011 Antarctic winter, conducted a simulation with two modes of NAT particles with number density of 0.0001 cm^{-3} and 5 cm^{-3} in WACCM PSC parameterization. It uses the NAT with 0.0001 cm^{-3} number density for denitrification purpose. Another possible cause of the underestimation of denitrification in the WACCM case simulation is a warm temperature bias of ~1–2 K in MERRA reanalysis over the polar area compared with the MLS temperature (Brakebusch et al., 2013). The previous studies indicate that the temperature bias strongly influences denitrification when we simulate the Arctic (Zhu et al., 2015), and it influences the heterogeneous chemistry and increases ozone depletion in both polar areas (Solomon et al., 2015; Zhu et al., 2015).

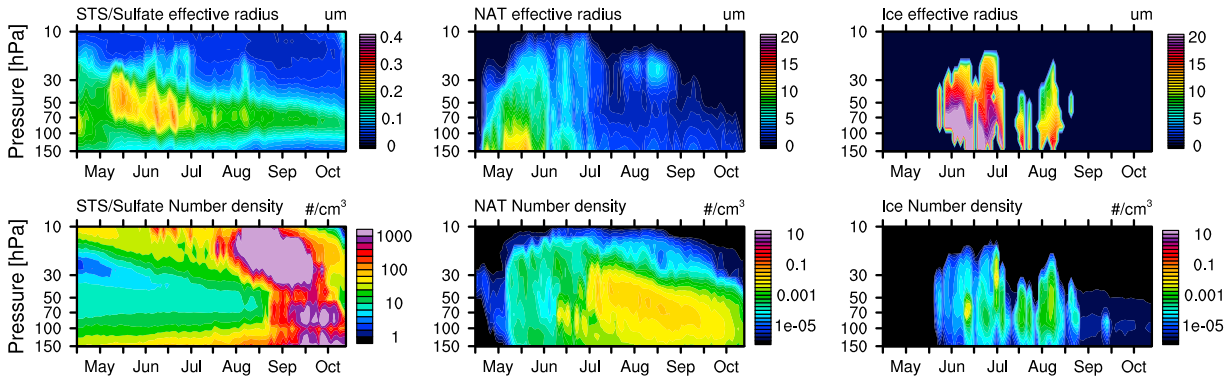

Figure 16. Base case: (top) STS, NAT, and ice effective radius and (bottom) the number density from May to October 2010. These are the 80°S–82°S average values.

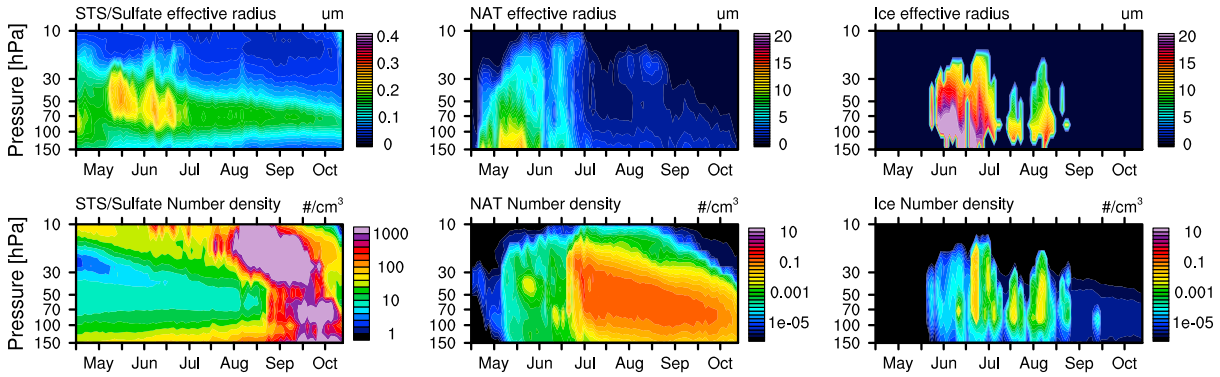

Figure 17. Wave case: (top) STS, NAT, and ice effective radius and (bottom) the number density from May to October 2010. These are the 80°S–82°S average values.

We conduct a test case with −1.5 K temperature adjustment applied in the WACCM/CARMA model for both PSC microphysics and heterogeneous chemical reactions as described by Zhu et al. (2015) for this winter. It overestimates both temporary denitrification and dehydration from late May to the end of September at all pressure levels compared with MLS observations.

We also compute the effective radius and number density of STS, NAT, and ice averaged for 80°S–82°S. Figures 16 and 17 show the two model case comparisons. The STS in the two cases are similar in May

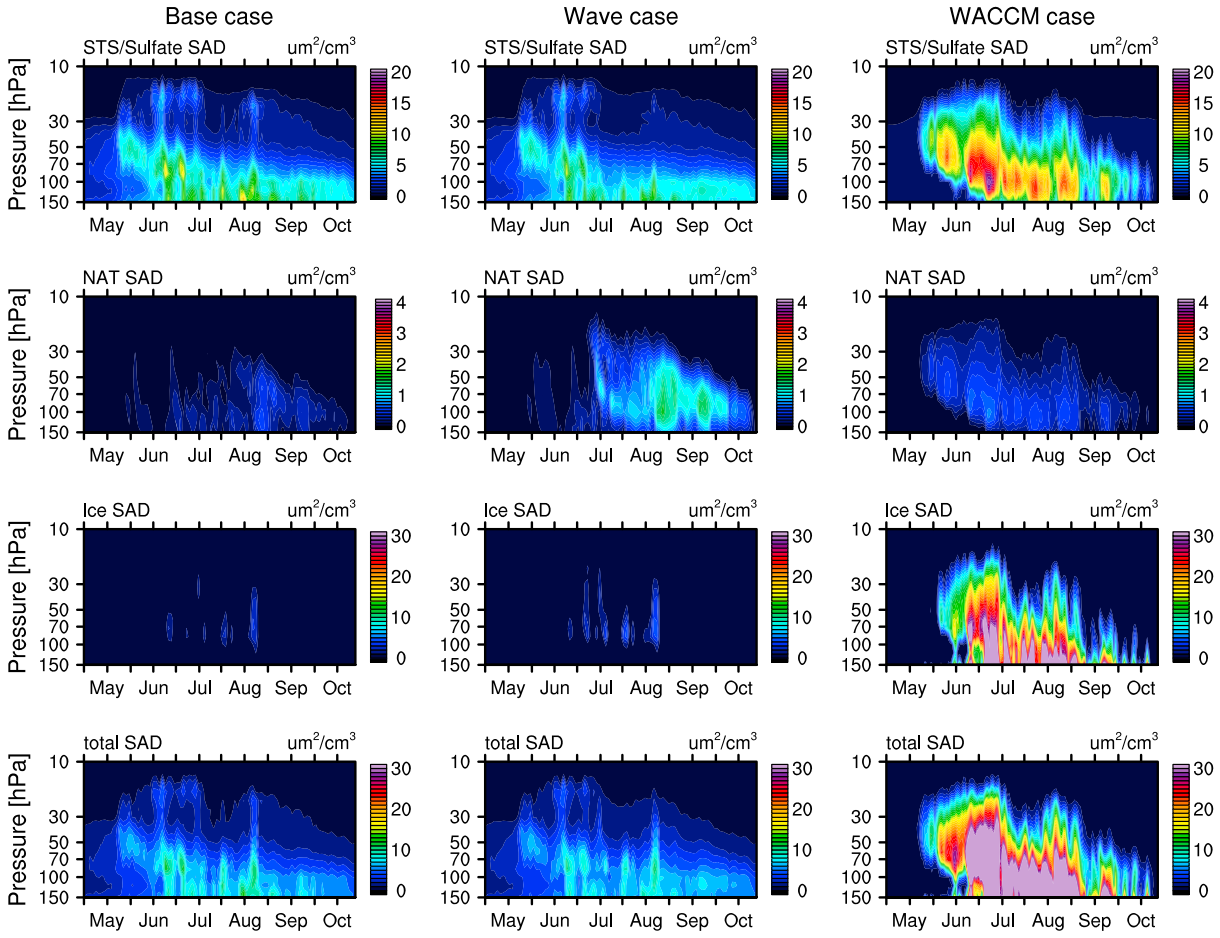

Figure 18. The surface area density (SAD) of STS, NAT, ice, and total PSCs from the modeled base case, wave case, and the WACCM case in 2010 Antarctic winter and spring. The SAD is averaged from 80°S to 82°S.

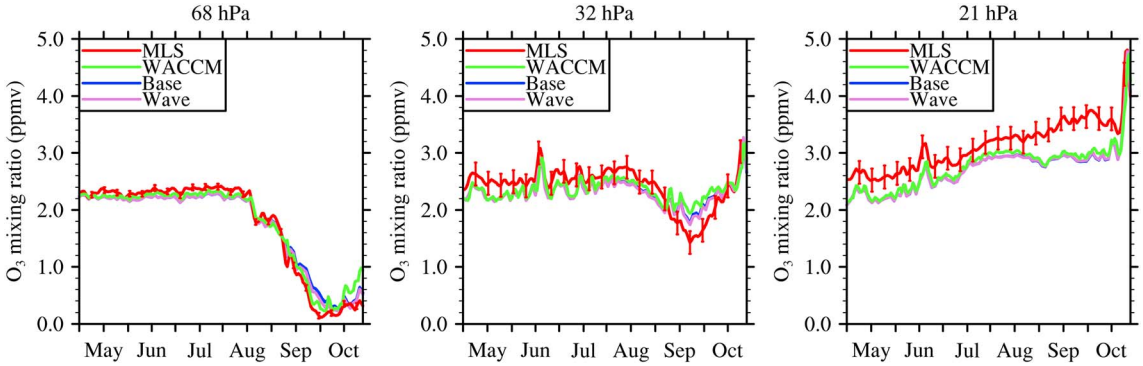

Figure 19. The average ozone mixing ratio from 80°S to 82°S evolution at different pressure levels during 2010 Antarctic winter and spring.

and June. The STS effective radius in the base case is slightly larger in July and August compared with the wave case. In both cases, NAT generally has a large effective radius in May and June and the effective radius decreases rapidly starting in July and continuing until October. When waves are introduced the NAT number density increases by 1 order of magnitude from July to October while the effective radius decreases. The ice effective radius in the base case is slightly larger compared with the wave case, while the number density of ice in the base case is about 1 order of magnitude smaller. It should be noted that as the STS/sulfate aerosols' effective radius falls and the number increases significantly (over 1000 cm^{-3}) from August to October in Figures 16 and 17, the surface area density (SAD) goes down slightly in Figure 18. This pattern occurs because there are very large numbers of very small particles with low surface area being generated by nucleation of sulfates. Or to put it another way the number density multiplied by the effective radius squared cannot be used to determine the SAD, one has to actually do the integrals over the size distribution.

4.5. Ozone

PSCs provide the surface area for chorine activation and therefore deplete the ozone in the springtime. Figure 18 compares the surface area densities from our simulations and the WACCM case's surface area density parameterizations. Figure 18 shows that the NAT and ice surface area densities increase in midwinter and later when waves are present. The STS/sulfate surface area decreases slightly in the wave case compared with the base case. In total, the base case and the wave case have similar surface area densities. The WACCM case has very different surface area density distributions, especially the ice. In total, the surface area density in the WACCM case is over 3 times higher than in our CARMA PSC cases.

Figure 19 shows the ozone mixing ratios from the MLS observations, the simulation from the WACCM case (labeled as WACCM), the base case, and the wave case from May to October, 2010. The three simulated cases start with slightly lower ozone than the MLS observation at all pressure levels. However, the simulations are within the observations' error bars in September and October at 68 hPa and 32 hPa. The base case (blue) and the wave case (purple) almost overlap each other. Generally, the three simulated cases are very similar with their ozone predictions even though the surface area densities shown in Figure 18 are quite different. As discussed in Solomon et al. (2015), if the heterogeneous chemistry acts only on liquid particles but not on water ice, the ozone depletion is nearly identical with the case with both liquid particles and ice. This indicates that the surface area provided by the PSCs in the base case is enough to activate the chorine to deplete the ozone. The O_3 at 21 hPa from the model cases in Figure 19 is outside the MLS error bars after late August. There may be several reasons for this error. First, the O_3 initial condition at this level is about 0.4 ppmv lower than the observation, which is one of the factors causing the underestimation of O_3. However, the trend of O_3 shows that the modeled O_3 flattens out over the Antarctic spring time (September and October), while the observed O_3 keeps increasing. Solomon et al. (2015) show that the standard WACCM model depletes 20% of O_3 near 21 hPa for 2011 Antarctic winter due to heterogeneous chemistry. It is possible that our model has some O_3 depletion going on due to PSC formation and chlorine activation at this pressure level, whereas the observations have near zero. It is unlikely that the error is due to vertical transport (descending air) because the simulated N_2O (Figure 14) shows good agreement with the observations.

5. Conclusion

This paper investigates the features of PSCs and their related vapors during the 2010 Antarctic winter. We discuss size distributions of NAT and ice particles, PSC optical properties, denitrification, dehydration, and ozone evolution. We also compare these features with and without introducing temperature fluctuations into the model due to gravity waves. We list the five questions we sought to answer.

The answers to question 1 are the following:

Previous studies indicate that both large NAT and small NAT particles are observed in the Antarctic winter (Eckermann et al., 2009; Höpfner et al., 2006; Lambert et al., 2012). In the previous version of our PSC model, in which NAT only forms from STS through homogeneous nucleation, we find that the model only forms large NAT particles that contribute to the denitrification but do not produce the backscattering ratios often observed by CALIPSO in midwinter in Antarctica (Zhu et al., 2017). In the current model version, we are able to produce small NAT particles in midwinter in the Antarctic by adding heterogeneous nucleation of NAT from ice particles. Figure 3 shows the probability distribution function of NAT effective radius at different time periods. At 52 hPa, the simulations only produce large NAT particles ~8 μm on 27 May because ice rarely forms in previous days. However, both large (~8 μm) and small NAT particles (submicrometers to a few micrometers) are simulated on 10 and 16 July, because both STS and ice form near the Antarctic Peninsula in previous days. On 22 July, only small NAT particles exist because STS rarely forms in previous days.

The answers to question 2 are the following:

On 24 to 28 May, the model produces NAT with large sizes and small number densities, showing low backscattering ratio ~1.5 over Ross Ice Sheet, which is consistent with CALIPSO observation in the same area. CALIPSO also observes a small number of PSCs classified in Mix2-enhanced and ice categories. However, the model does not reproduce this feature in either base case or wave case. This error might be due to several factors that might cause thermal perturbations such as small-scale gravity waves, unrealistic large-scale temperature fluctuations, or nonorographic gravity waves.

On 18 to 22 July, the model produces NAT with large backscattering ratio downwind of the Antarctic Peninsula. Adding waves increases the backscattering ratio from NAT and ice. But CALIPSO shows a higher backscattering ratio than simulated, which may indicate that a better wave representation is needed.

The answers to question 3 are the following:

The simulated H_2O evolution is within the error bars of MLS H_2O observations in the lower stratosphere. Both the simulations and the observations at 80°S show dehydration starting from early June.

The simulated HNO_3 evolution varies from case to case. The addition of waves increases the denitrification but predicts too much denitrification at 21 hPa in August. Comparing to the WACCM parameterization, our PSC model improves the HNO_3 prediction because the number density of NAT is assumed to be 10^{-2} cm^3 and the calculated size of NAT is generally smaller than 2 μm in the WACCM PSC parameterization. We suggest the WACCM PSC parameterization should assume a bimodal size distribution of NAT particles.

The answers to question 4 are the following:

Mountain waves decrease the size of ice and NAT particles. Smaller particles have increased backscatter, which is more consistent with CALIPSO observations. Smaller ice particles do not change the H_2O evolution very much but smaller nitric acid particles do increase the denitrification. Compared with the wave case with ±2 K, increasing the amplitude of temperature fluctuations to ±3 K or ±4 K increases the backscattering ratio from NAT and ice particles and produces better comparisons with CALIPSO backscattering ratio in July. A small amount of the ice mixtures with backscattering ratio higher than 5 are produced in ±4 K case, where the CALIPSO shows a backscattering ratio of 6. However, increasing the amplitude also leads to a strong overestimation of denitrification around 21 hPa in August compared with MLS observations. In the similar way, ±1 K scenario produces better denitrification at 21 hPa but poorer backscatter in July. Therefore, we choose ±2 K as the wave case in this paper.

The answers to question 5 are the following:

The modeled ozone is lower than MLS observation in the winter but is within the error bars of MLS observations in the springtime. Adding waves to the model does not change the ozone amount very much, which

indicates that the surface areas provided by PSCs in the base case in the model are enough to active the chorine to deplete the ozone.

Temperature fluctuations are important to produce ice particles with large number densities. A better wave representation is necessary to produce PSCs with the high backscattering ratios observed by CALIPSO. Further work is needed to determine if a more accurate gravity wave parameterization would improve ozone forecasts.

Acknowledgments
The work at the University of Colorado was supported by NASA grant NNX09AK71G from the AURA satellite project, NASA grant NNX16AQ37G, and National Science Foundation (NSF) grant PLR1643701. The work at the Jet Propulsion Laboratory, California Institute of Technology, was carried out under a contract with the National Aeronautics and Space Administration. The National Center for Atmospheric Research (NCAR) is sponsored by the U.S. National Science Foundation (NSF). WACCM is a component of NCAR's Community Earth System Model (CESM), which is supported by NSF and the Office of Science of the U.S. Department of Energy. We would like to acknowledge high-performance computing support from Yellowstone (ark:/85065/d7wd3xhc) and Cheyenne (doi:10.5065/D6RX99HX) provided by NCAR's Computational and Information Systems Laboratory (CISL), sponsored by the NSF. The source code for WACCM/CARMA model used in this study is freely available at http://www2.cesm.ucar.edu/ upon registration. The developing version of this model, the data, and input files necessary to reproduce the experiments are available from the authors upon request (yunqian.zhu@colorado.edu). The data are archived at the Toon Aerosol Research Group computers.

References

Alexander, S. P., Klekociuk, A. R., McDonald, A. J., & Pitts, M. C. (2013). Quantifying the role of orographic gravity waves on polar stratospheric cloud occurrence in the Antarctic and the Arctic. *Journal of Geophysical Research: Atmospheres*, *118*, 11,493–11,507. https://doi.org/10.1002/2013JD020122

Brakebusch, M., Randall, C. E., Kinnison, D. E., Tilmes, S., Santee, M. L., & Manney, G. L. (2013). Evaluation of Whole Atmosphere Community Climate Model simulations of ozone during Arctic winter 2004–2005. *Journal of Geophysical Research: Atmospheres*, *118*, 2673–2688. https://doi.org/10.1002/jgrd.50226

Carslaw, K. S., Luo, B. P., Clegg, S. L., Peter, T., Brimblecombe, P., & Crutzen, P. J. (1994). Stratospheric aerosol growth and HNO_3 gas phase depletion from coupled HNO_3 and water uptake by liquid particles. *Geophysical Research Letters*, *21*(23), 2479–2482. https://doi.org/10.1029/94GL02799

Carslaw, K. S., Wirth, M., Tsias, A., Luo, B. P., Dörnbrack, A., Leutbecher, M., … Peter, T. (1998a). Particle microphysics and chemistry in remotely observed mountain polar stratospheric clouds. *Journal of Geophysical Research: Atmospheres*, *103*(D5), 5785–5796. https://doi.org/10.1029/97JD03626

Carslaw, K. S., Wirth, M., Tsias, A., Luo, B. P., Dörnbrack, A., Leutbecher, M., … Peter, T. (1998b). Increased stratospheric ozone depletion due to mountain-induced atmospheric waves. *Nature*, *391*(6668), 675–678. https://doi.org/10.1038/35589

de Laat, A. T. J., & van Weele, M. (2011). The 2010 Antarctic ozone hole: Observed reduction in ozone destruction by minor sudden stratospheric warmings. *Scientific Reports*, *1*, 1–8. https://doi.org/10.1038/srep00038

Eckermann, S. D., Hoffmann, L., Höpfner, M., Wu, D. L., & Alexander, M. J. (2009). Antarctic NAT PSC belt of June 2003: Observational validation of the mountain wave seeding hypothesis. *Geophysical Research Letters*, *36*, L02807. https://doi.org/10.1029/2008GL036629

Engel, I., Luo, B. P., Pitts, M. C., Poole, L. R., Hoyle, C. R., Grooß, J.-U., … Peter, T. (2013). Heterogeneous formation of polar stratospheric clouds—Part 2: Nucleation of ice on synoptic scales. *Atmospheric Chemistry and Physics*, *13*, 10,769–10,785. https://doi.org/10.5194/acp-13-10769-2013

English, J. M., Toon, O. B., Mills, M. J., & Yu, F. (2011). Microphysical simulations of new particle formation in the upper troposphere and lower stratosphere. *Atmospheric Chemistry and Physics*, *11*(17), 9303–9322. https://doi.org/10.5194/acp-11-9303-2011

Fueglistaler, S., Luo, B. P., Voigt, C., Carslaw, K. S., & Peter, T. (2002). NAT-rock formation by mother clouds: A microphysical model study. *Atmospheric Chemistry and Physics*, *2*(2), 93–98. https://doi.org/10.5194/acp-2-93-2002

Garcia, R. R., Marsh, D. R., Kinnison, D. E., Boville, B. A., & Sassi, F. (2007). Simulation of secular trends in the middle atmosphere, 1950–2003. *Journal of Geophysical Research: Atmospheres*, *112*, D09301. https://doi.org/10.1029/2006JD007485

Hanson, D., & Mauersberger, K. (1988). Laboratory studies of the nitric acid trihydrate: Implications for the south polar stratosphere. *Geophysical Research Letters*, *15*(8), 855–858. https://doi.org/10.1029/GL015i008p00855

Höpfner, M., Blumenstock, T., Hase, F., Zimmermann, A., Flentje, H., & Fueglistaler, S. (2001). Mountain polar stratospheric cloud measurements by Ground Based FTIR Solar Absorption Spectroscopy. *Geophysical Research Letters*, *28*(11), 2189–2192. https://doi.org/10.1029/2000GL012841

Höpfner, M., Larsen, N., Spang, R., Luo, B. P., Ma, J., Svendsen, S. H., … Fischer, H. (2006). MIPAS detects Antarctic stratospheric belt of NAT PSCs caused by mountain waves. *Atmospheric Chemistry and Physics*, *6*(5), 1221–1230. https://doi.org/10.5194/acp-6-1221-2006

Kinnison, D. E., Brasseur, G. P., Walters, S., Garcia, R. R., Marsh, D. R., Sassi, F., … Simmons, A. (2007). Sensitivity of chemical tracers to meteorological parameters in the MOZART-3 chemical transport model. *Journal of Geophysical Research*, *112*, D20302. https://doi.org/10.1029/2006JD007879

Koop, T., Luo, B., Tsias, A., & Peter, T. (2000). Water activity as the determinant for homogeneous ice nucleation in aqueous solutions. *Nature*, *406*(6796), 611–614.

Kunz, A., Pan, L. L., Konopka, P., Kinnison, D. E., & Tilmes, S. (2011). Chemical and dynamical discontinuity at the extratropical tropopause based on START08 and WACCM analyses. *Journal of Geophysical Research*, *116*, D24302. https://doi.org/10.1029/2011JD016686

Lamarque, J.-F., Emmons, L. K., Hess, P. G., Kinnison, D. E., Tilmes, S., Vitt, F., … Tyndall, G. K. (2012). CAM-chem: Description and evaluation of interactive atmospheric chemistry in the Community Earth System Model. *Geoscientific Model Development*, *5*(2), 369–411. https://doi.org/10.5194/gmd-5-369-2012

Lambert, A., Santee, M. L., Wu, D. L., & Chae, J. H. (2012). A-train CALIOP and MLS observations of early winter Antarctic polar stratospheric clouds and nitric acid in 2008. *Atmospheric Chemistry and Physics*, *12*(6), 2899–2931.

Livesey, N. J., Read, W. G., Froidevaux, L., Lambert, A., Manney, G. L., Pumphrey, H. C., … Cofield, R. E. (2011). Version 3.3 level 2 data quality and description document, *JPL D-33509*.

Luo, B., Carslaw, K. S., Peter, T., & Clegg, S. L. (1995). Vapour pressures of $H_2SO_4/HNO_3/HCl/HBr/H_2O$ solutions to low stratospheric temperatures. *Geophysical Research Letters*, *22*(3), 247–250. https://doi.org/10.1029/94GL02988

Marsh, D. R., Mills, M. J., Kinnison, D. E., Lamarque, J.-F., Calvo, N., & Polvani, L. M. (2013). Climate change from 1850 to 2005 simulated in CESM1 (WACCM). *Journal of Climate*, *26*(19), 7372–7391. https://doi.org/10.1175/JCLI-D-12-00558.1

Mishchenko, M. I., & Travis, L. D. (1998). Capabilities and limitations of a current FORTRAN implementation of the T-matrix method for randomly oriented, rotationally symmetric scatterers. *Journal of Quantitative Spectroscopy and Radiation Transfer*, *60*(3), 309–324. https://doi.org/10.1016/S0022-4073(98)00008-9

Murphy, D. M., & Koop, T. (2005). Review of the vapour pressures of ice and supercooled water for atmospheric applications. *Quarterly Journal of the Royal Meteorological Society*, *131*(608), 1539–1565.

Noel, V., & Pitts, M. (2012). Gravity wave events from mesoscale simulations, compared to polar stratospheric clouds observed from spaceborne lidar over the Antarctic Peninsula. *Journal of Geophysical Research*, *117*, D11207. https://doi.org/10.1029/2011JD017318

Pitts, M. C., Poole, L. R., Lambert, A., & Thomason, L. W. (2013). An assessment of CALIOP polar stratospheric cloud composition classification. *Atmospheric Chemistry and Physics*, *13*(6), 2975–2988. https://doi.org/10.5194/acp-13-2975-2013

Pitts, M. C., Poole, L. R., & Thomason, L. W. (2009). CALIPSO polar stratospheric cloud observations: Second-generation detection algorithm and composition discrimination. *Atmospheric Chemistry and Physics*, *9*(19), 7577–7589. https://doi.org/10.5194/acp-9-7577-2009

Pitts, M. C., Thomason, L. W., Poole, L. R., & Winker, D. M. (2007). Characterization of polar stratospheric clouds with spaceborne lidar: CALIPSO and the 2006 Antarctic season. *Atmospheric Chemistry and Physics*, *7*(19), 5207–5228. https://doi.org/10.5194/acp-7-5207-2007

Podglajen, A., Hertzog, A., Plougonven, R., & Legras, B. (2016). Lagrangian temperature and vertical velocity fluctuations due to gravity waves in the lower stratosphere. *Geophysical Research Letters*, *43*, 3543–3553. https://doi.org/10.1002/2016GL068148

Poole, L. R., & McCormick, M. P. (1988). Airborne lidar observations of Arctic polar stratospheric clouds: Indications of two distinct growth stages. *Geophysical Research Letters*, *15*(1), 21–23. https://doi.org/10.1029/GL015i001p00021

Pruppacher, H. R., & Klett, J. D. (1997). *Microphysics of clouds and precipitation* (2nd ed.). Dordrecht, Boston: Kluwer Academic Publishers.

Rienecker, M. M., Suarez, M. J., Gelaro, R., Todling, R., Bacmeister, J., Liu, E., … Woollen, J. (2011). MERRA: NASA's Modern-Era Retrospective Analysis for Research and Applications. *Journal of Climate*, *24*(14), 3624–3648. https://doi.org/10.1175/JCLI-D-11-00015.1

Schoeberl, M. R. (2007). The EOS Aura mission. In *Observing systems for atmospheric composition* (pp. 64–70). New York: Springer.

Shibata, T., Sato, K., Kobayashi, H., Yabuki, M., & Shiobara, M. (2003). Antarctic polar stratospheric clouds under temperature perturbation by nonorographic inertia gravity waves observed by micropulse lidar at Syowa station, *Journal of Geophysical Research: Atmospheres*, *108*(D3), 4105. https://doi.org/10.1029/2002JD002713.

Solomon, S., Garcia, R. R., Rowland, F. S., & Wuebbles, D. J. (1986). On the depletion of Antarctic ozone. *Nature*, *321*(6072), 755–758.

Solomon, S., Kinnison, D., Bandoro, J., & Garcia, R. (2015). Simulation of polar ozone depletion: An update. *Journal of Geophysical Research: Atmospheres*, *120*, 7958–7974. https://doi.org/10.1002/2015JD023365

Toon, O. B., Turco, R. P., Jordan, J., Goodman, J., & Ferry, G. (1989). Physical processes in polar stratospheric ice clouds. *Journal of Geophysical Research: Atmospheres*, *94*(D9), 11,359–11,380. https://doi.org/10.1029/JD094iD09p11359

Turco, R. P., Toon, O. B., & Hamill, P. (1989). Heterogeneous physicochemistry of the polar ozone hole. *Journal of Geophysical Research: Atmospheres*, *94*(D14), 16,493–16,510. https://doi.org/10.1029/JD094iD14p16493

Wegner, T., Kinnison, D. E., Garcia, R. R., & Solomon, S. (2013). Simulation of polar stratospheric clouds in the specified dynamics version of the whole atmosphere community climate model. *Journal of Geophysical Research: Atmospheres*, *118*, 4991–5002. https://doi.org/10.1002/jgrd.50415

Winker, D. M., Hunt, W. H., & McGill, M. J. (2007). Initial performance assessment of CALIOP. *Geophysical Research Letters*, *34*, L19803. https://doi.org/10.1029/2007GL030135

Zhu, Y., Toon, O. B., Lambert, A., Kinnison, D. E., Brakebusch, M., Bardeen, C. G., … English, J. M. (2015). Development of a polar stratospheric cloud model within the Community Earth System Model using constraints on type I PSCs from the 2010–2011 Arctic winter. *Journal of Advances in Modeling Earth Systems*, *7*, 551–585. https://doi.org/10.1002/2015MS000427

Zhu, Y., Toon, O. B., Pitts, M. C., Lambert, A., Bardeen, C., & Kinnison, D. E. (2017). Comparing simulated PSC optical properties with CALIPSO observations during the 2010 Antarctic winter. *Journal of Geophysical Research: Atmospheres*, *122*, 1175–1202. https://doi.org/10.1002/2016JD025191